# ôMobile Radar Observations of the Evolving Debris Field Compared with a Damage Survey of the Shawnee, Oklahoma, Tornado of 19 May 2013<sup>♠</sup>

### ROGER M. WAKIMOTO

Department of Atmospheric and Oceanic Sciences, University of California, Los Angeles, Los Angeles, California

#### ZACHARY WIENHOFF AND HOWARD B. BLUESTEIN

School of Meteorology, University of Oklahoma, Norman, Oklahoma

### DAVID J. BODINE AND JAMES M. KURDZO

Advanced Radar Research Center, Norman, Oklahoma

(Manuscript received 24 June 2019, in final form 15 February 2020)

#### ABSTRACT

A detailed damage survey is combined with high-resolution mobile, rapid-scanning X-band polarimetric radar data collected on the Shawnee, Oklahoma, tornado of 19 May 2013. The focus of this study is the radar data collected during a period when the tornado was producing damage rated EF3. Vertical profiles of mobile radar data, centered on the tornado, revealed that the radar reflectivity was approximately uniform with height and increased in magnitude as more debris was lofted. There was a large decrease in both the cross-correlation coefficient ( $\rho_{\rm hv}$ ) and differential radar reflectivity ( $Z_{\rm DR}$ ) immediately after the tornado exited the damaged area rated EF3. Low  $\rho_{\rm hv}$  and  $Z_{\rm DR}$  occurred near the surface where debris loading was the greatest. The 10th percentile of  $\rho_{\rm hv}$  decreased markedly after large amounts of debris were lofted after the tornado leveled a number of structures. Subsequently,  $\rho_{\rm hv}$  quickly recovered to higher values. This recovery suggests that the largest debris had been centrifuged or fallen out whereas light debris remained or continued to be lofted. Range–height profiles of the dual-Doppler analyses that were azimuthally averaged around the tornado revealed a zone of maximum radial convergence at a smaller radius relative to the leading edge of lofted debris. Low-level inflow into the tornado encountering a positive bias in the tornado-relative radial velocities could explain the existence of the zone. The vertical structure of the convergence zone was shown for the first time.

#### 1. Introduction

Lofted debris surrounding the funnel cloud is a characteristic feature of many tornadoes. In addition to being visually impressive, debris can impact the tornado's wind field by reducing the azimuthal velocities (e.g., Lewellen et al. 2008; Bodine et al. 2016b). This decrease,

Oenotes content that is immediately available upon publication as open access.

© Supplemental information related to this paper is available at the Journals Online website: https://doi.org/10.1175/MWR-D-19-0215.s1.

Corresponding author: Roger M. Wakimoto, wakimotoroger@gmail.com

however, does not imply that damage potential has been reduced. Total swirl momentum including debris loading can increase and airborne projectiles and sandblasting can produce even greater damage potential and be a major contributor to the destruction of structures observed along the tornado track (e.g., Doswell and Brooks 2002; Lewellen et al. 2008). Although the importance of lofted debris in tornadoes is well-recognized, there have been no detailed observational studies published in the literature that have shown the evolution of large debris originating from damaged structures and its impact on the wind field using polarimetric data. Specifically, high temporal resolution polarimetric data are needed to characterize the debris field evolution since large debris fall out faster due to larger terminal velocities (Dowell et al. 2005).

Data collected by ground-based, mobile Doppler radars have been invaluable in revealing the finescale

DOI: 10.1175/MWR-D-19-0215.1

structure of tornadoes such as suction vortices and improved definition of the low-level wind field (e.g., Wurman and Gill 2000; Wurman 2002; Bluestein et al. 2004, 2007a, 2015, 2018, 2019; Lee and Wurman 2005; Kosiba and Wurman 2010; Wakimoto et al. 2011; Wurman and Kosiba 2013; Wurman et al. 2013, 2014; Kurdzo et al. 2017). More recently, discrimination between hydrometeors and regions of lofted debris is possible with the addition of polarimetric measurements (e.g., Ryzhkov et al. 2005; Bluestein et al. 2007b, 2015, 2019; Kumjian and Ryzhkov 2008; Bodine et al. 2013, 2014; Snyder and Bluestein 2014; Kurdzo et al. 2015; Houser et al. 2016; Tanamachi et al. 2012; Wakimoto et al. 2015, 2016; Mahre et al. 2018). The tornadic debris signature (TDS) was first proposed by Ryzhkov et al. (2005) <sup>1</sup> to approximately delineate lofted debris based on high equivalent radar reflectivity factor,<sup>2</sup> low differential radar reflectivity  $(Z_{DR})$ , and low cross-correlation coefficient  $(\rho_{hv})$  that are collocated with the tornadic rotational couplet observed in radial velocity. Regions characterized by low  $\rho_{hv}$  have been generally accepted as one of the better indicators of lofted debris (e.g., Bodine et al. 2014; Van Den Broeke 2015; Houser et al. 2016). Low  $Z_{DR}$  can also be used to locate regions of lofted debris; however,  $Z_{DR}$  can exhibit a positive bias when rain is present (e.g., Bluestein et al. 2007b) and a negative bias in the presence of resonance scattering and/or common debris alignment (Ryzhkov et al. 2005; Bluestein et al. 2007b; Cheong et al. 2017; Umeyama et al. 2018). Low values of  $Z_{\rm DR}$  can also be due to differential attenuation if downrange from a heavy precipitation core (Schultz et al. 2012a).

The intense circulation associated with tornadoes results in strong centrifuging of hydrometeors and debris (e.g., Dowell et al. 2005). This centrifuging can produce a positive bias in the tornado-relative radial velocities relative to the airspeed since Doppler radars are measuring the motion of the scatterers (e.g., Dowell et al. 2005; Wakimoto et al. 2012; Nolan 2013; Bodine et al. 2014). The bias can lead to an anomalous divergent signature in Doppler velocities within the tornado at low levels where centrifuging is typically the most intense owing to a combination of larger debris particles and the strongest rotational velocities (e.g., Dowell et al. 2005). Indeed, many rotational couplets do not suggest strong

low-level convergence in contrast to numerical simulations and laboratory experiments of intense vortices (e.g., Lewellen et al. 2008).

Several studies have attempted to relate TDS characteristics to tornado damage (e.g., Ryzhkov et al. 2005; Schultz et al. 2012b; Bodine et al. 2013, 2014; Van Den Broeke and Jauernic 2014; Van Den Broeke 2015). Schultz et al. (2012a) noted that definitive relationships between EF rating and TDSs were not possible unless it was known what was damaged, when it was damaged, and the degree to which it was damaged. Van Den Broeke and Jauernic (2014) used the Storm Events Database maintained by the National Centers for Environmental Information (https://www.ncdc.noaa.gov/stormevents/), which has been shown to have limitations (Trapp et al. 2006). While the database is the best available resource on tornadic events across the nation, the information can poorly characterize the scope and magnitude of the surveyed damage. Indeed, the reports can underrepresent a significant event in terms of both property damage and areal coverage of damage. There are also examples of reports that overrepresent a relatively less significant event. Bodine et al. (2013) compared TDS parameters recorded by nearby Weather Surveillance Radar-1988 Doppler (WSR-88D) radars with two National Weather Service (NWS) damage surveys of strong tornadoes. The TDS parameters correlated well with the enhanced Fujita (EF) scale. However, the poor temporal resolution of the volume scans associated with the WSR-88D and the long distance from the radar to parts of the tornado track were limiting factors. Van Den Broeke and Jauernic (2014) used land-cover data provided by the U.S. Geological Survey (USGS) to document the characteristics of the ground; however, the data may not be the most accurate in areas that are changing either due to construction or farming, which alters the landscape over a period of a few days/weeks. Van Den Broeke (2015) suggested that land cover changes may produce noticeable differences in the TDS when the tornado is near a radar. His analysis contains some comparisons with reported damage. In one case, a drop in  $\rho_{hv}$  occurs after a tornado produced intense damage.

The present study presents a unique analysis of highresolution polarimetric data of a TDS associated with an intense tornado near Shawnee, Oklahoma. The data collection period of the radar included a period when the tornado was lofting large amounts of debris from a number of structures identified during comprehensive aerial and ground surveys. The evolution of the lofted debris field is documented with both single and dual-Doppler analyses in greater detail than previous studies. The latter analysis was able to resolve, for the first time,

<sup>&</sup>lt;sup>1</sup> Giangrande (2002), Ryzhkov et al. (2002), and Schuur et al. (2004) summarized observations of tornadic debris signatures in the nonrefereed literature.

<sup>&</sup>lt;sup>2</sup> Equivalent radar reflectivity factor assumes that the scatterers are comprised of small, spherical liquid drops whose backscattering cross sections can be described by the Rayleigh approximation; hereafter, referred to as radar reflectivity.

### Shawnee Tornadoes May 19, 2013

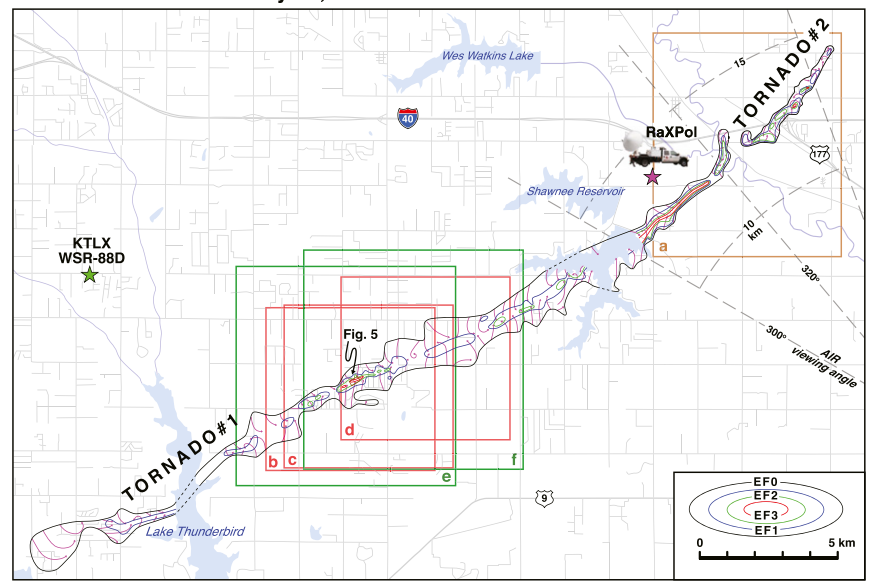


FIG. 1. Damage map of the Shawnee, Oklahoma, tornadoes on 19 May 2013. Isopleths denote the EF damage intensity. Magenta lines represent the approximate flow as depicted in the damage based on fallen trees and building debris observed during the poststorm ground and aerial surveys. Green and magenta stars represent the locations of the KTLX WSR-88D and RaXPol radars, respectively. Azimuth angle and range rings for the AIR radar are shown as dashed lines. Photographs of tornado 1 were taken from the RaXPol site. Area enclosed by the brown box is shown in Figs. 3 and 4. Red boxes are analysis areas that are shown in Figs. 6, 9, and 12. Green boxes denote the locations of dual-Doppler analyses that are shown in Figs. 16 and 17. Black arrow denotes the location of the detailed damage map shown in Figs. 5.

the vertical structure of the "false" convergence zone, which forms as a result of debris centrifuging from the tornado encountering low-level inflow into the circulation. Section 2 describes the radar platforms, the dual-Doppler wind synthesis, and photogrammetric analyses used in the current study. Section 3 presents the results of the surveys of the tornado damage. A comparison of the data collected by RaXPol and a dual-Doppler analysis with the damage survey is presented in section 4. Section 5 presents a discussion and summary.

# 2. Radar data, dual-Doppler analysis, and photogrammetry

The mobile, rapid-scanning X-band polarimetric Doppler radar (RaXPol; Pazmany et al. 2013) was the primary platform used in the present study. RaXPol is a mobile, rapid-scanning polarimetric radar that transmits radiation at a wavelength of 3.1 cm. The half-power beamwidth is 1° and the antenna diameter is 2.4 m. The antenna is capable of rotating as rapidly as  $180^{\circ} \, \text{s}^{-1}$ . The range resolution is 30 m oversampled such that the range gates were 15 m. A frequency-diversity technique known as frequency hopping is implemented to increase the number of independent samples needed to calculate

the radar variables while in rapid scan mode (e.g., Hildebrand and Moore 1990). The interested reader is referred to Pazmany et al. (2013) for additional information on RaXPol. The Shawnee tornado was also scanned by the KTLX WSR-88D radar that provided an opportunity to perform dual-Doppler wind syntheses (Fig. 1). RaXPol scanned the tornado from 2301–2321 UTC (UTC = CDT + 5 h) while deployed at the site shown in Fig. 1. Wienhoff et al. (2018) also produced dual-Doppler analyses of the circulation using the KTLX and RaXPol radars on this day.

The Atmospheric Imaging Radar (AIR; Isom et al. 2013) was also deployed on this day and was located southeast of the tornado (Fig. 1) and collected radar reflectivity images of the hook echo accompanying the tornado (Kurdzo et al. 2017). AIR operates at X band and uses a technique known as digital beamforming. The antenna transmits a horizontally polarized vertical fan beam that is 1° in azimuth and 20° in elevation. The data from all elevations are recorded simultaneously resulting in "pseudo" RHIs. The antenna is mechanically steered in azimuth. The AIR only collected radar reflectivity data on 19 May.

The locations of the dual-Doppler wind syntheses are shown by the boxes labeled "e" and "f" in Fig. 1.

The grid spacing for the analysis is 200 m and is based on the lowest spatial resolution in the analysis domain. The tornado was moving at  $\sim$ 12.4 m s  $^{-1}$  from 250° during the analysis times. A two-pass Barnes filter (Barnes 1964) was applied using a smoothing parameter  $\kappa = (1.33\Delta)^2$ , where  $\Delta$  equals the grid spacing (Pauley and Wu 1990). The response function resulted in 30% and 10% of the energy at wavelengths equal to and less than 0.95 and 0.70 km, respectively, being damped. The interested reader is referred to Majcen et al. (2008) for additional information regarding the filtering process. The tornado-relative wind field is presented in the figures.

Several pictures of the wall cloud associated with the Shawnee supercell were analyzed using photogrammetric techniques. Photogrammetry can be used to analyze photos quantitatively to determine angular measurements that can be converted into horizontal and vertical dimensions at the distance of a phenomenon of interest (e.g., Malkus 1952; Wakimoto and Martner 1992; Zehnder et al. 2007). An example of a photogrammetric analysis for the current study will be presented in section 4a.

### 3. The damage survey

The Shawnee tornado formed at ~2300 UTC near Lake Thunderbird and moved northeast over Shawnee Reservoir before dissipating near Highway 177 and Interstate 40 just northwest of Shawnee, Oklahoma (Fig. 1). The tornado passed through heavily forested regions but also moved through several neighborhoods. A number of structures were severely damaged or destroyed. Additional aspects of the Shawnee tornado are presented by Wienhoff (2016).

The result presented in Fig. 1 is based on ground surveys followed by an aerial survey using a Cessna aircraft of the Shawnee tornado track on 22, 23, and 24 May (Fig. 1). The tornado was rated EF3 based on damage to a number of structures along its path. This damage intensity rating differs from the NWS survey (https://www.weather.gov/oun/events-20130519-ef4tornado), which rated the tornado as EF4. The lead author could not identify any damage indicators that would support the EF4 rating over the region shown in the NWS map. Numerous fallen trees, debris swaths and damage marks on the ground were carefully plotted during the survey. The damage survey revealed that there were two separate tornadoes rather than the one reported in the Storm Events Database. The first tornado formed southwest of Lake Thunderbird and moved to the northeast until making a "left turn" (e.g., Fujita 1974) to the north before dissipating when it reached Interstate 40. The total pathlength was ~29.5 km. An aerial photo of the left turn is shown in Fig. 2. A second tornado, also rated EF3, formed less than 1 km to the east of the end of the tornado 1, moved northeastward to near the intersection of Interstate 40 and Highway 177 and continued for ~3 km before dissipating (Fig. 3). The relatively short distance separating the end of the track of tornado 1 and the beginning of tornado 2 led to the initial assessment by the NWS that the track was continuous (NWS 2013, personal communication).

Radar reflectivity images recorded by AIR at the 2° elevation-angle scan revealed that the hook echo made a loop-like trajectory between the dissipation of tornado 1 and formation of tornado 2. The height of the radar beam was  $\sim$ 440 m ARL (above radar level; hereafter, all heights are ARL). An example of one of the AIR scans is shown in Fig. 4 and a movie of the loop can be found in the online supplemental material.<sup>3</sup> The rapid nature of cyclic tornadogenesis (∼1 min between the dissipation of tornado 1 and the formation of tornado 2) is noteworthy and would require rapid-scan radars to fully document. There has been recent interest in small looping movements of circulations that can lead to cusp-like tornado tracks (Kurdzo et al. 2015; see their Fig. 14) or, in the present study, cyclic tornadoes. Cyclic tornadoes have been described by several researchers (e.g., Burgess et al. 1982; Dowell and Bluestein 2002; Adlerman and Droegemeier 2005; Houser et al. 2015). The rear flank gust front starts an occlusion process by surging around the updraft and tornado, resulting in a weaker circulation and movement to the north. A new circulation typically develops farther south along the gust front and, subsequently, another tornado forms. More research is required to understand the difference between the current case study and "failed occlusion" (Kurdzo et al. 2015) that resulted in a loop in the Moore tornado track.

An example of the finescale analysis of the damage in an area rated EF3 is shown in Fig. 5. The location of the rotational couplet at 2316:42 UTC is shown in the figure. The region was characterized by fallen trees, large piles of debris from buildings that were destroyed, and numerous pieces of lumber that were primarily aligned in a direction that was consistent with the debris streaks and downed trees. The alignment of

 $<sup>^3</sup>$  The location of the weak-echo hole outside of the damage track in the figure is likely a result of the height of the height of the beam above the radar level ( $\sim$ 440 m) combined with the vertical tilt in the tornado circulation.

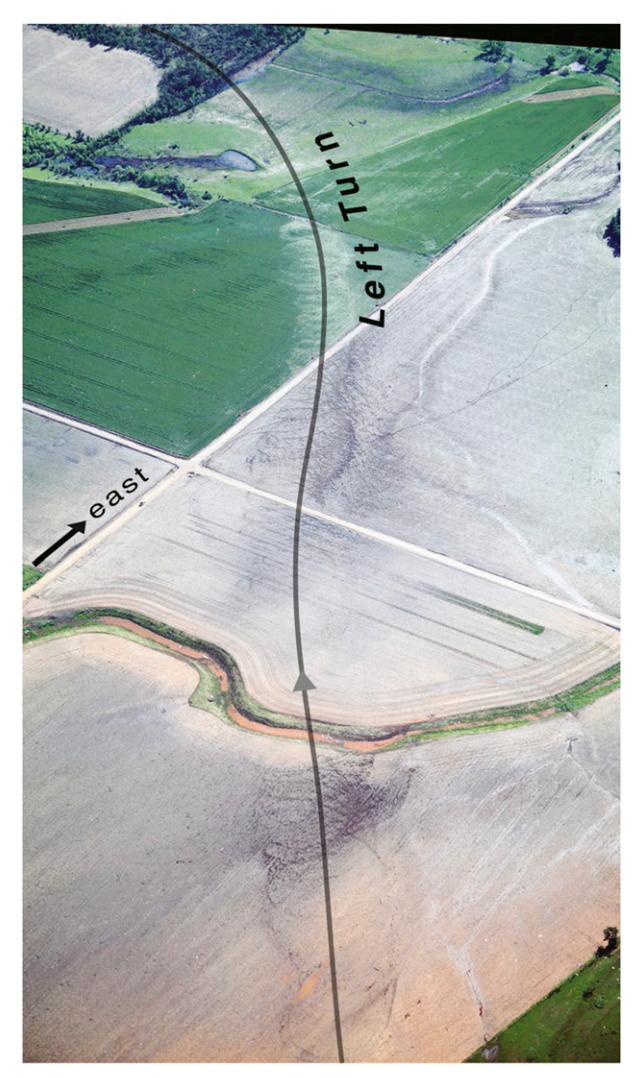


FIG. 2. Aerial photo near the end of the Shawnee tornado track 1. The tornado made a "left turn" at the end of the track until it was heading in a northerly direction. The area presented in this figure is enclosed by the brown box in Fig. 3.

lumber with the wind direction is consistent with the simulated findings of Umeyama et al. (2018). It is apparent in the photo that debris from several structures became airborne and were deposited ~100 m downwind in large piles. The clustering of debris downstream from its source region suggests that most of the debris was lofted at the same time and followed a similar trajectory before being deposited. A row of trees approximately 130 and 50 m in length and width, respectively, was uprooted or snapped off by the tornado resulting in a large treeless gap (highlighted by the magenta line in Fig. 5). The damage in the area depicted in the figure is illustrative of the source for debris particles lofted by the tornado.

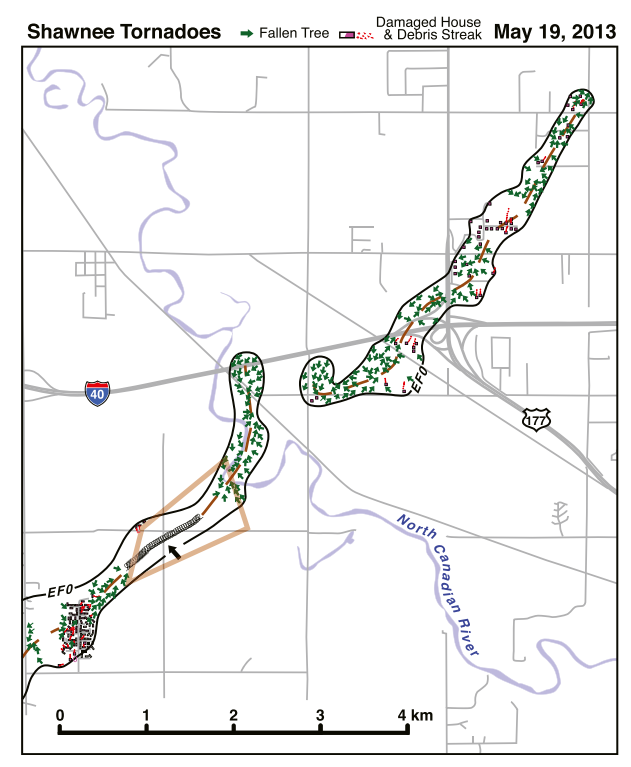


FIG. 3. Damage map of the end of tornado 1 and the beginning of tornado 2. Fallen trees and damaged houses/debris streak are shown by the arrows and squares, respectively. Orange dashed line represents the center of the tornado tracks. The isopleth of EFO damage is shown by the black line. Black arrow denotes a region where a series of looping marks were apparent in a field. The area enclosed by the brown box is shown in Fig. 2. The area shown in this figure is enclosed by the brown box labeled "a" in Fig. 1.

# 4. Radar observations of the debris field compared with the damage survey

## a. RaXPol radar observations compared with the damage survey

RaXPol collected data from 2301-2321 UTC at the site shown in in Fig. 1. The time period 2316:10–2320: 26 UTC was chosen for analysis for two reasons. The tornado was located ~13.5 km southwest of the radar site at ~2316 UTC resulting in the collection of highresolution polarimetric data at low levels. In addition, the time interval selected encompasses a period when the Shawnee tornado produced damage rated EF3 as it demolished a number of homes (Figs. 1 and 5). Equivalent damage intensity was not identified at earlier times. The red box labeled "b" in Fig. 1 is enlarged in Fig. 6. The tornado was not visible from the RaXPol site at 2316:15 UTC; however, a prominent wall cloud  $(\sim 1.9 \,\mathrm{km}$  diameter) could be identified in the photographs (Fig. 6e). The angular dimension of the wall cloud is shown by the blue circle in Figs. 6a-d.

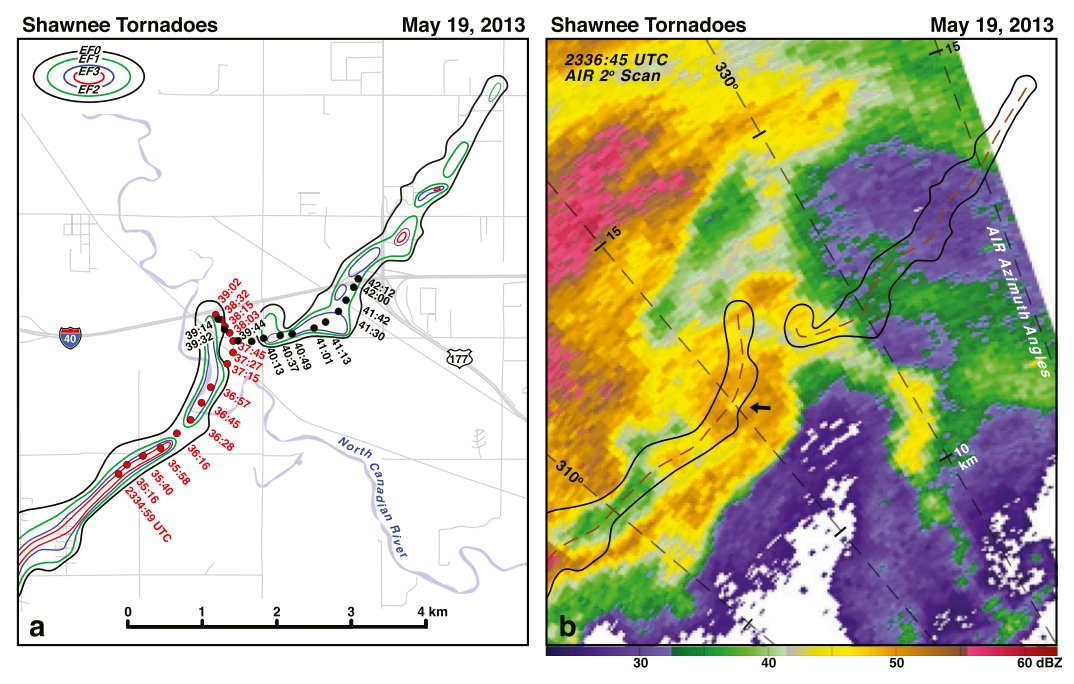


FIG. 4. (a) Damage map of the two tornadoes with the location and times of the weak-echo hole within the hook echo as determined by AIR depicted. The red and black dots are used in order to more easily track the locations of the weak-echo hole. EF isopleths of damage intensity are shown. (b) Radar reflectivity image at 2° from AIR at 2336:45 UTC. The EF0 isopleths (black lines) and the center of the tornado track (brown dashed line) are depicted. Black arrow denotes the location of the weak-echo hole. The area shown is enclosed by the brown box labeled "a" in Fig. 1.

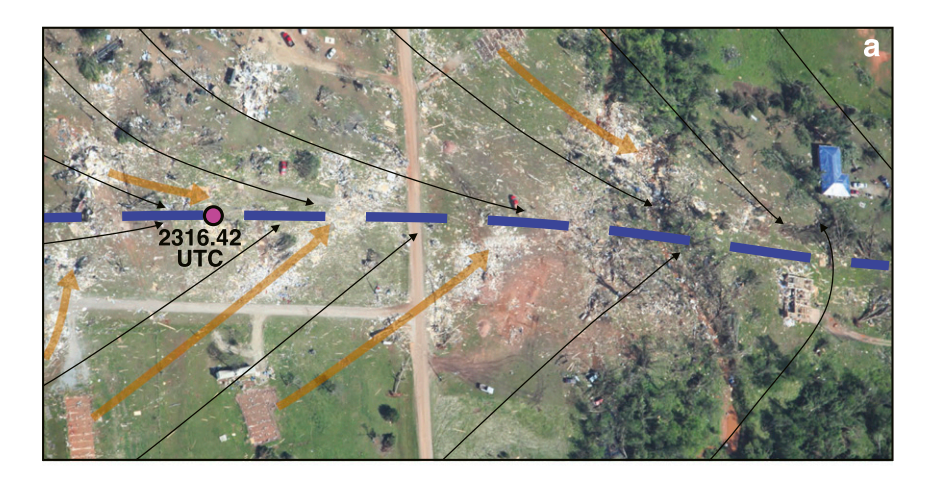
The tornado was displaced to the south of the center of the wall cloud (Figs. 6a, c, and e). The magenta line in Figs. 6a-c represents the outline of the TDS based on the area of low  $\rho_{hv}$  (Fig. 6d). Not surprisingly, the TDS is also located in the southern part of the wall cloud. The northern and southern extents of the TDS and the location of the tornado are indicated on the picture (Fig. 6e). The rotational couplet at 3° elevation angle (Fig. 6c) is centered within the TDS. The 3° elevation was chosen since it provided the best depiction of the TDS.<sup>4</sup> Data from other elevation angles will be presented later in the text. A band of high radar reflectivity wrapping around the circulation is apparent in Fig. 6b. The collocation of the band with relatively high  $\rho_{hv}$  and  $Z_{\rm DR}$  (not shown) suggests that it is most likely composed of precipitation.

An enlargement of the dashed boxed-in area (Figs. 6a–d) is presented in Fig. 7. A more detailed analysis of the damage along the tornado track reveals a small area rated EF3 near the location of the tornado at 2316: 10 UTC (Fig. 7a) and a much larger area of EF3 damage

to the northeast where significant debris was lofted between 2316:42 and 2317:15 UTC. The rotational couplet (Fig. 7c) accompanies the hook echo (Fig. 7b) and is associated with a debris signature (Fig. 7d). The maximum radar reflectivities within the hook echo are located in the southwest quadrant. The rotational couplet does not suggest the presence of strong convergence as illustrated in the damage survey (e.g., Fig. 5). Its absence is related to several factors. The Doppler radar measurements cannot resolve smaller-scale features such as corner flow present in a tornado. The 3° elevation angle of the scan may not capture the convergent flow occurring at the lowest levels. Finally, debris centrifuging results in a false divergence signature that could mask the low-level convergence that may be present. The radius of maximum tangential winds associated with the tornado would also be difficult to resolve using radar measurements.

The challenge of performing comprehensive damage surveys is illustrated in Fig. 8. Both analyses shown in the figure include the information compiled from the detailed aerial and ground survey. The only difference between the plots shown in Figs. 8a and 8b are the isopleths of EF damage. The former is based on the detailed survey while the latter is based on the

 $<sup>^4</sup>$  The height of the TDS at 3° ranges from 550 to 700 m in this paper.



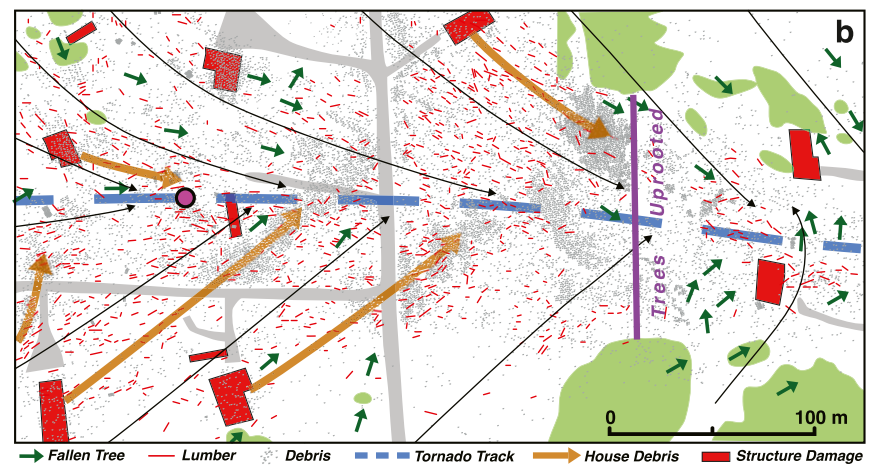


FIG. 5. (a) Aerial photo of damage caused by the Shawnee tornado. (b) Damage map of the tornado track covering the same region as shown in (a). Green arrows represent fallen trees. Red lines represent the locations of lumber from structures that were damaged. Gray dots represent individual debris particles. Red shaded areas denote parts of structures that were damaged. Dashed blue line represents the center of the tornado track in both panels. Brown lines represent the trajectory of debris from houses that were destroyed in both panels. Black lines represent the approximate flow as depicted in the damage based on fallen trees, building debris, and numerous pieces of lumber scattered in the fields in both panels. The region highlighted by the magenta line is a row of trees that was destroyed with all trees in the region uprooted or snapped off by the tornado. The location of the rotation couplet at 2316:42 UTC based on data recorded by RaXPol is shown by the magenta circle. The location of the area presented in this figure is shown in Figs. 1, 7, and 10.

NWS analysis (https://www.weather.gov/oun/events-20130519-ef4tornado). There are no areas rated EF3 in the latter even though the results shown in Fig. 5 revealed intense damage to a number of structures and to regions of dense forests that were leveled. The authors propose that understanding the evolution of the TDS is closely related to the ground characteristics and the accuracy of the damage intensity analysis.

The tornado continued to damage a number of structures in an area rated EF3 at 2317:20 UTC (Figs. 9 and 10). There is a slight reduction in the areal extent of the TDS (cf. Fig. 7d with Fig. 10d); however, there has

been an increase in the maximum radar reflectivities within the TDS (Fig. 10b) in response to the lofted debris in the region shown in Fig. 5 (similar increases in radar reflectivity after debris lofting has been noted by Kurdzo et al. 2017). The area of maximum velocities away from the radar has decreased when compared with the previous analysis time (Figs. 7c and 10c) and may be a result of increased debris loading (e.g., Lewellen et al. 2008; Bodine et al. 2016b). The support for higher debris loading is the increase in radar reflectivities that has occurred in the northwestern section of the hook echo (Fig. 10b) where the decrease in Doppler velocities has

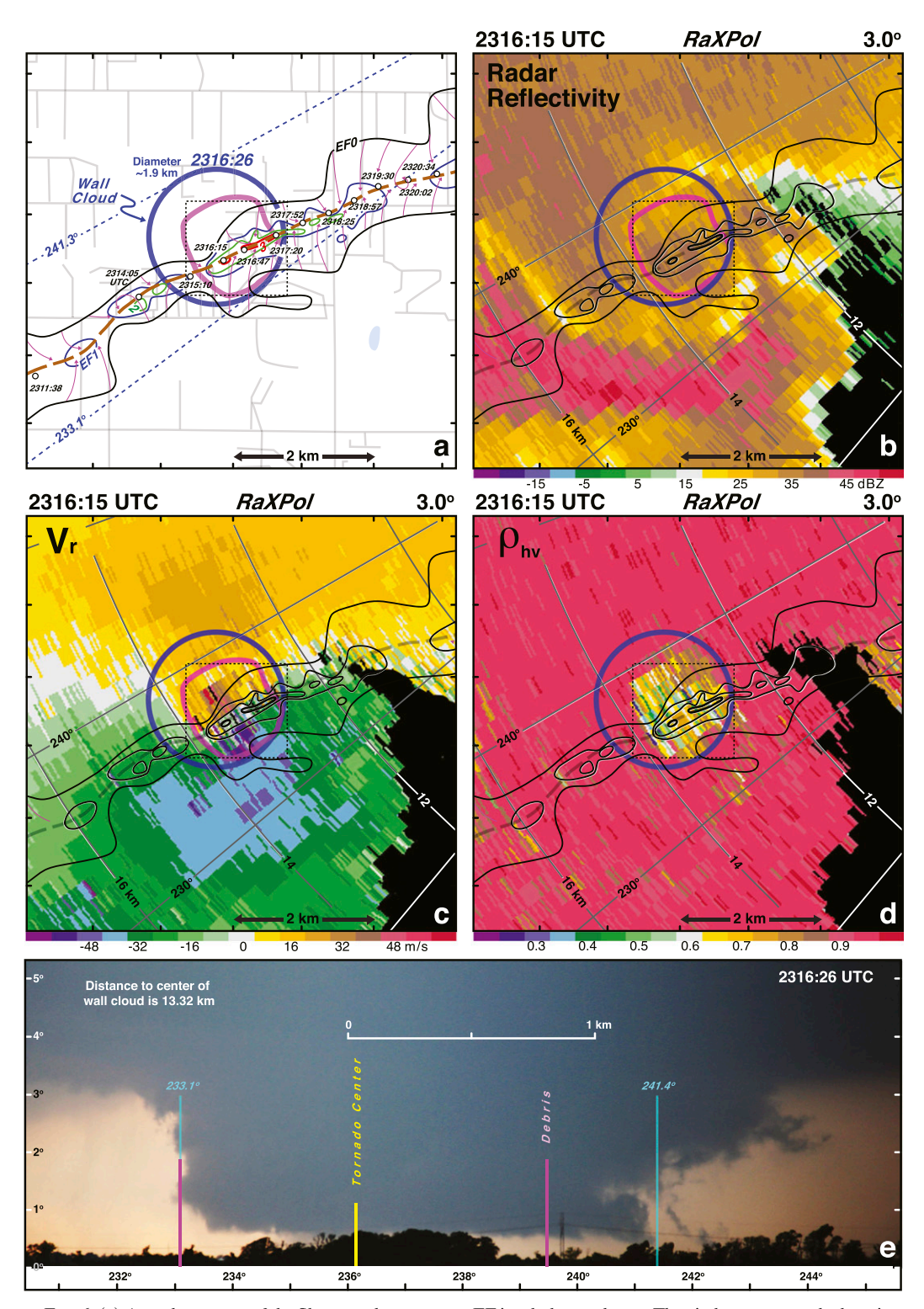


FIG. 6. (a) An enlargement of the Shawnee damage map. EF isopleths are drawn. The circles represent the location of the center of the rotational couplet at the indicated times. Dashed brown line denotes the center of the tornado track. Thin magenta lines represent the approximate direction of the flow based on debris streaks, fallen trees, and striation marks in the fields. Dashed blue lines are the azimuths from RaXPol and are shown in (e). (b) Radar reflectivity scan, (c) Doppler velocity scan, and (d) cross-correlation coefficient scan at 3° from RaXPol at 2316:15 UTC. Thick magenta line in (a)–(c) and blue circle in (a)–(d) represent the approximate outline of the area of low  $\rho_{hv}$  and

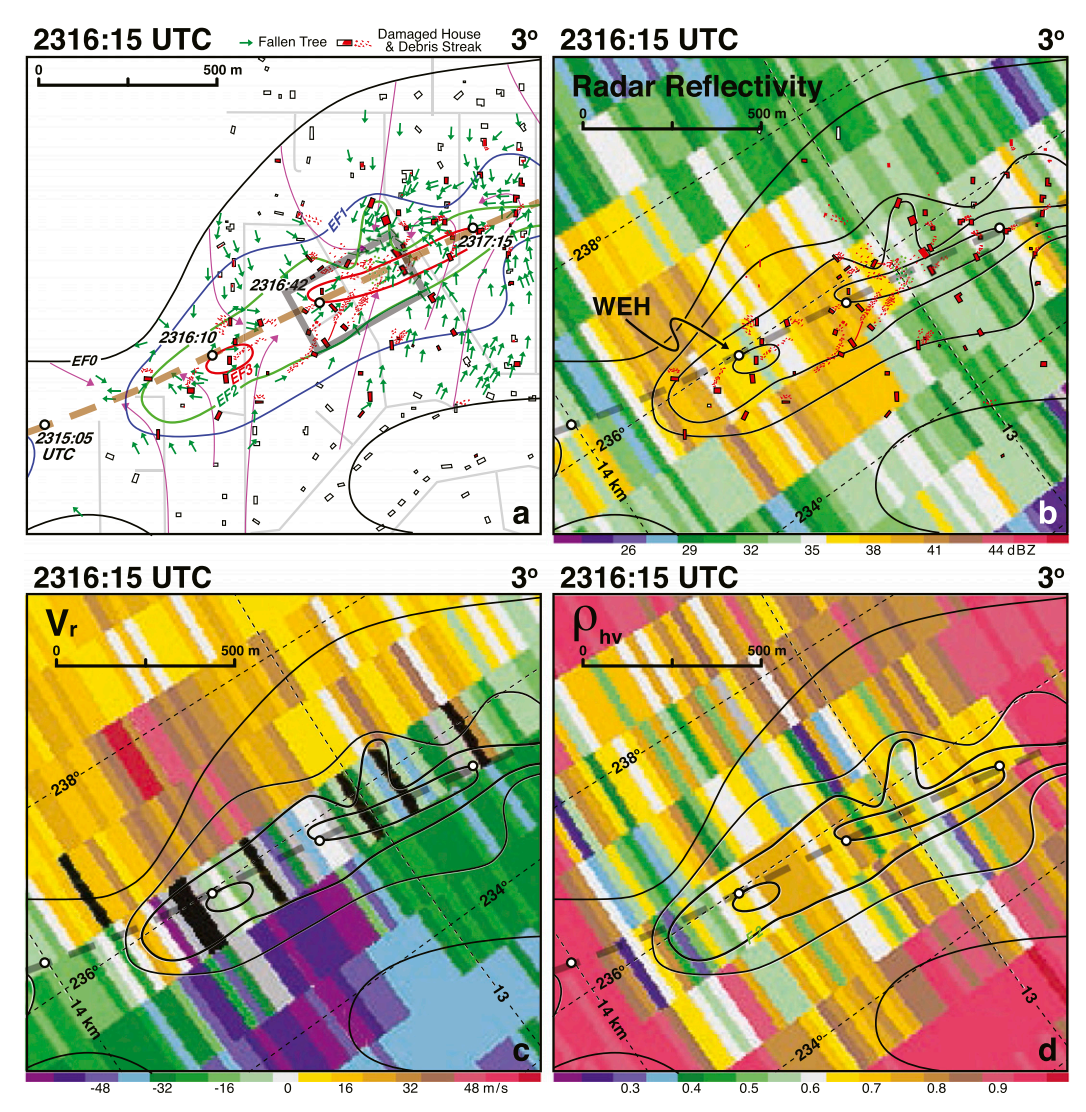


FIG. 7. (a) Detailed damage map of the Shawnee tornado. EF isopleths are drawn. The circles represent the location of the center of the rotational couplet at the indicated times. Dashed brown line denotes the center of the tornado track. Damaged and undamaged houses are distinguished by the white and red shading, respectively. Streaks of house debris are shown. Thin magenta lines represent the approximate direction of the flow based on debris streaks, fallen trees (green arrows), and striation marks in the fields. Gray box is enlarged in Fig. 5. (b) Radar reflectivity scan at 3° from RaXPol at 2316:15 UTC. Damage analysis of the houses is also shown. (c) Doppler velocity scan at 3° from RaXPol at 2316:15 UTC. (d) Cross-correlation coefficient scan at 3° from RaXPol at 2316:15 UTC. Area in (a)–(d) is enclosed by the dashed black box shown in Fig. 6. Black pixels denote velocities that have been removed based on large spectral widths.

occurred (Fig. 10c). The radar reflectivity within the hook echo continues to increase at 2318:57 UTC as more of the lofted debris is entrained into the circulation even though the tornado had entered a forested area largely devoid of

structures (Figs. 11a,b). The beam height is ~600 m at this time. The TDS has grown in areal extent (Figs. 11c,d) in response to the centrifuging of large debris that has been lofted. It is likely that leaves from trees were still being

 $\leftarrow$ 

the wall cloud, respectively. (e) Photograph of the wall cloud at 2316:26 UTC. Blue and magenta lines denote the approximate azimuthal dimensions of the wall cloud and low  $\rho_{hv}$  signature, respectively. The yellow line represents the approximate center of the Shawnee tornado. The length scale is valid at the distance of the center of the wall cloud. Area shown in (a)–(d) is enclosed by the red box labeled "b" in Fig. 1. The dashed black box is enlarged in Fig. 7.

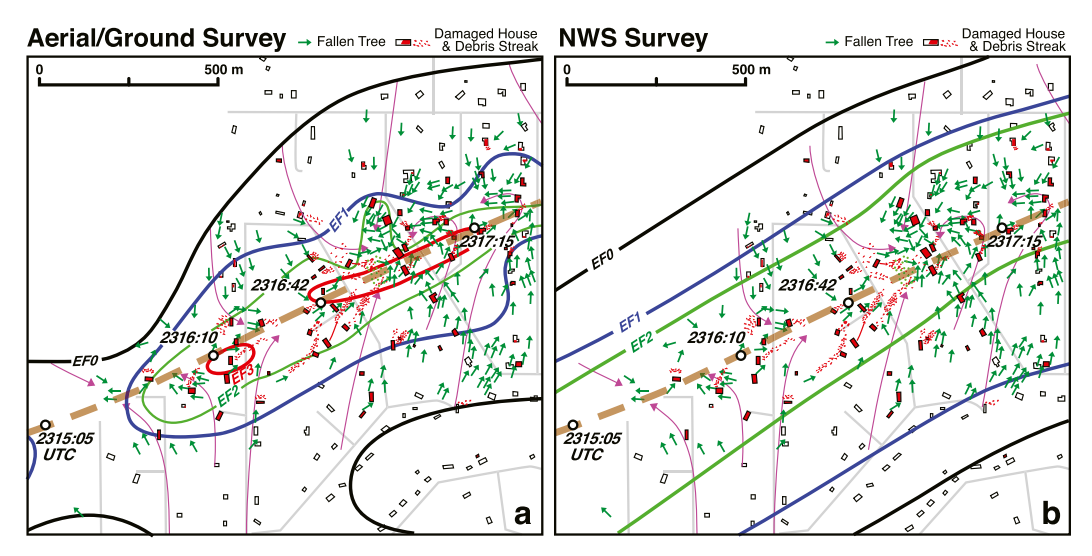


FIG. 8. Detailed damage map of the Shawnee tornado (a) based on aerial and ground survey performed in the current study. (b) The same damage analysis presented in (a) but with the EF isopleths based on the official National Weather Service (NWS) survey. The circles represent the location of the center of the rotational couplet at the indicated times. Dashed brown line denotes the center of the tornado track. Damaged and undamaged houses are distinguished by the white and red shading, respectively. Streaks of house debris are shown. Thin magenta lines represent the approximate direction of the flow based on debris streaks, fallen trees (green arrows), and striation marks in the fields. Area in (a) and (b) is enclosed by the dashed black box shown in Fig. 6.

lofted in this region. The leaves would be lofted to a much higher level than the heavier debris from houses destroyed earlier. The outbound velocities are still reduced at this time.

Strong radar echoes are noted throughout the hook echo (Figs. 12b and 13b) and the TDS has grown in size at 2320:02 UTC, which may be related to the increase in tornado width as suggested by the damage path at this location (Fig. 12d). The tornado is centered over a region rated EF0 (Fig. 13a) suggesting that significant amounts of heavy debris are not being lofted from the surface. However, leaves from trees and other small particles from the ground are still being entrained into the tornadic circulation. The increase in debris loading within the tornado has not reduced the velocities within the rotational couplet. Instead, the difference of maximum velocities away and toward the radar has increased (cf. Figs. 11c and 13c). Simulations that introduce debris loading show an expected decrease in tornadic wind speeds when that is the only change involved (e.g., Lewellen et al. 2008). The analysis shown in Fig. 13c suggest that either the amount of debris was not sufficient to reduce the wind speeds of the tornado or that storm/tornado-scale processes that increased the tornado's intensity had a greater influence than any changes caused by debris loading. For example, Lewellen and Zimmerman (2008) have performed simulations of an intensifying tornado over a uniform debris field. More debris is lofted as the tornado velocities increase.

Time-height profiles of radar reflectivity, maximum difference between outbound and inbound velocities within the couplet ( $\Delta V_{\rm max}$ ),  $\rho_{\rm hv}$ , and  $Z_{\rm DR}$  for eight consecutive volume scans collected by RaXPol are presented in Fig. 14. The radar reflectivity,  $\rho_{hv}$ , and  $Z_{DR}$ plots were based on an areal average of the data out to a range of 1 km from the center of the rotational couplet. The maximum positive vertical vorticity was selected as the center for the areal average. Additional analyses were created for radii of 0.5 and 1.5 km. The former was deemed too noisy to use and the latter produced nearly identical plots to those shown in Figs. 14a, 14c, and 14d. The radar reflectivities at the lowest elevation angle are much weaker (Fig. 14a) owing to beam blockage by trees (Fig. 6e). At higher levels, the echoes are stronger and there is a general trend toward increasing radar reflectivity with time at all heights in response to the lofted debris from the damaged structures shown in Fig. 5. The radar reflectivities aloft are initially greater than 30 dBZ and approach  $\sim 40 \, \mathrm{dB}Z$  by the last volume scan as a result of large debris that was lofted from the earlier structural damage. There is little variation of radar reflectivity with height above the lowest elevation angle scan suggesting that the small debris becomes well mixed soon after it is lofted.

The vertical profile of  $\rho_{\rm hv}$  (Fig. 14c) is divided into two clusters below ~1.5 km. One set of profiles is clustered near 0.90 while the other half is clustered near 0.85. A noticeable reduction in  $\rho_{\rm hv}$  between 2317:47–2318:16

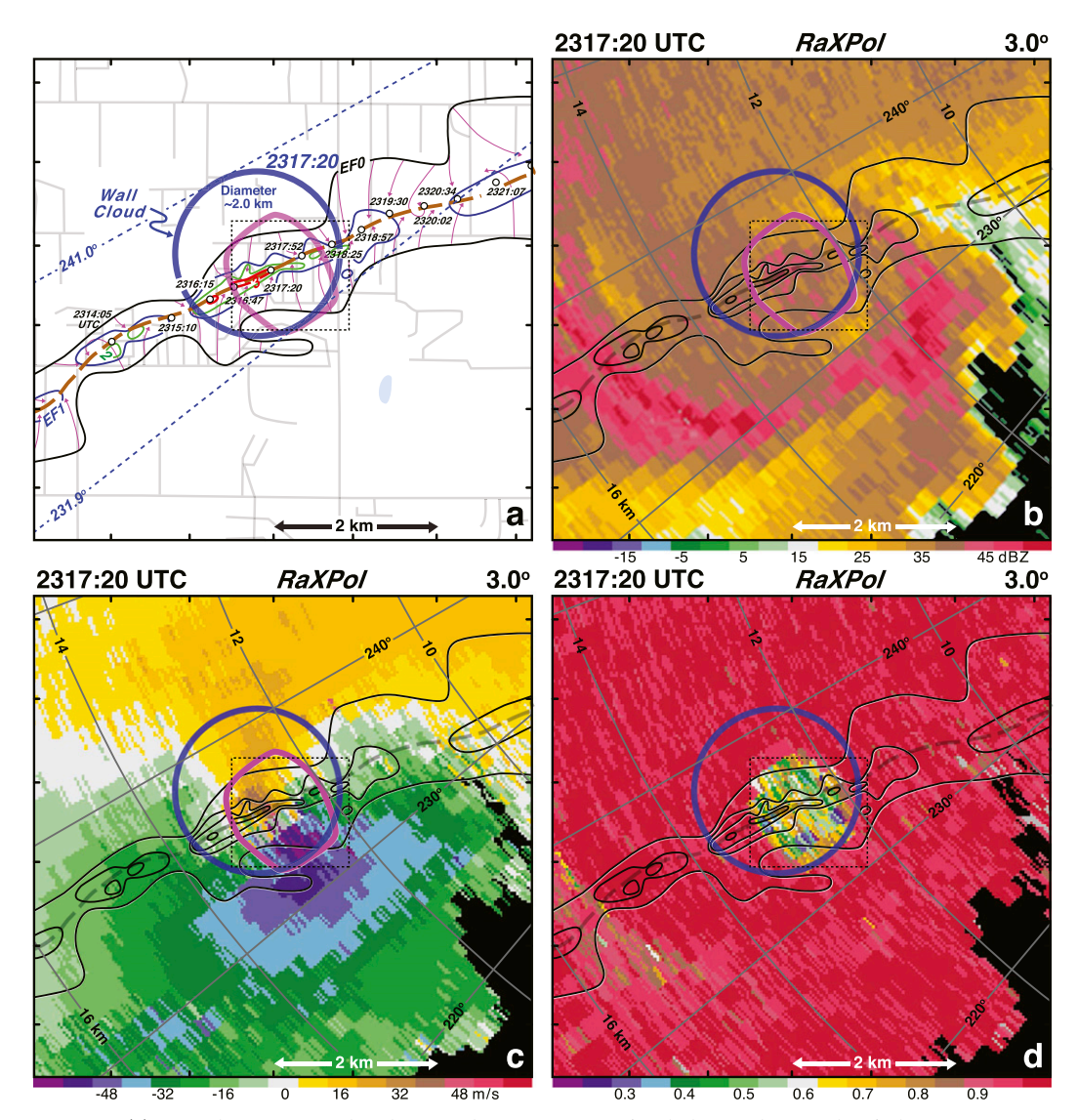


FIG. 9. (a) An enlargement of the Shawnee damage map. EF isopleths are drawn. The circles represent the location of the center of the rotational couplet at the indicated times. Dashed brown line denotes the center of the tornado track. Thin magenta lines represent the approximate direction of the flow based on debris streaks, fallen trees, and striation marks in the fields. Dashed blue lines are the azimuths from RaXPol. (b) Radar reflectivity scan, (c) Doppler velocity scan, and (d) cross-correlation coefficient scan at 3° from RaXPol at 2317:20 UTC. Thick magenta line in (a)–(c) and blue circle in (a)–(d) represent the approximate outline of the area of low  $\rho_{hv}$  and the wall cloud, respectively. Area shown in the figure is enclosed by the red box labeled "c" in Fig. 1. The dashed black box is enlarged in Fig. 10.

and 2318:23–2318:48 UTC is not accompanied by a large increase in radar reflectivity (Fig. 14a). This observation may suggest that the increase in lofted debris is primarily composed of small particles. Note that the fall in  $\rho_{\rm hv}$  occurs at ~2318 UTC, after the tornado was east of the area rated EF3 (e.g., Fig. 11). Low  $\rho_{\rm hv}$  occurs near the surface for all scan times (except 2318:23–2318:48 UTC) where the debris loading is large. The  $\rho_{\rm hv}$  value at the lowest elevation angle decreased from the 2317:15–2317: 44 to 2319:25–2319:54 UTC volumes. The  $\rho_{\rm hv}$  profiles

decrease with altitude between 1.5 and 2.5 km (Fig. 14c) that suggests increased lofted debris even though the radar reflectivity profiles in this region are relatively uniform with height (Fig. 14a). The minimum of  $\rho_{\rm hv}$  near 2.5 km in the later profiles may indicate a concentrated layer of debris. It is possible that the updraft may result in the accumulation of small debris at this height. Wakimoto et al. (2015) documented the existence of a debris overhang that was produced by an updraft. The trend of the profiles above 2.5 km is reversed.

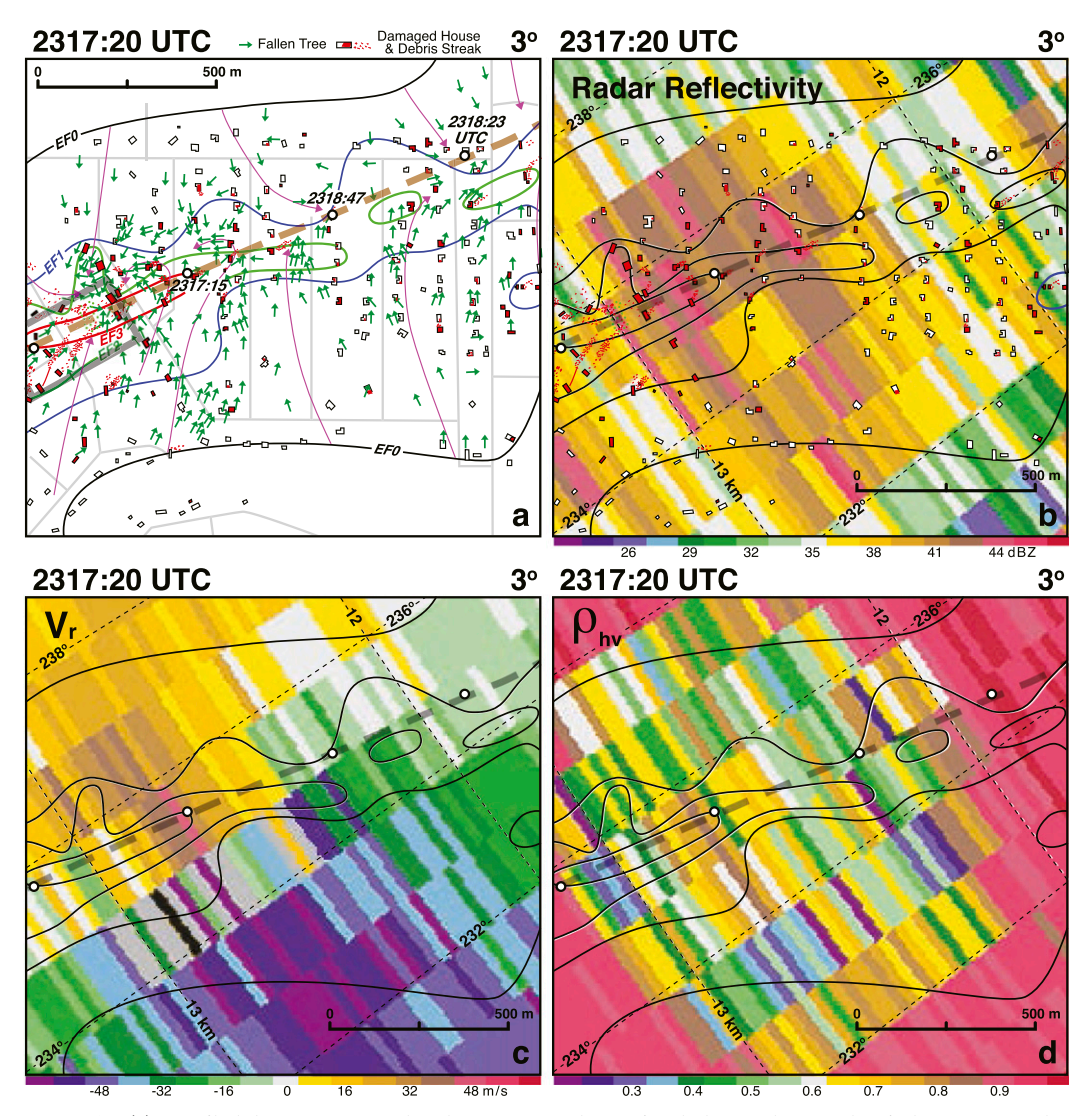


FIG. 10. (a) Detailed damage map of the Shawnee tornado. EF isopleths are drawn. The circles represent the location of the center of the rotational couplet at the indicated times. Dashed brown line denotes the center of the tornado track. Damaged and undamaged houses are distinguished by the white and red shading, respectively. Streaks of house debris are shown. Thin magenta lines represent the approximate direction of the flow based on debris streaks, fallen trees (green arrows), and striation marks in the fields. (b) Radar reflectivity scan at 3° from RaXPol at 2317:20 UTC. Damage analysis of the houses is also shown. (c) Doppler velocity scan at 3° from RaXPol at 2317:20 UTC. (d) Cross-correlation coefficient scan at 3° from RaXPol at 2317:20 UTC. Area in (a)–(d) is enclosed by the dashed black box shown in Fig. 9. Black pixel denotes a velocity value that has been removed based on large spectral widths.

Relatively high  $\rho_{\rm hv}$  is observed during the later volume scans. This trend suggests that the lofted debris at these heights has either been centrifuged or has fallen to lower levels. An increase in the velocity differential at these heights (Fig. 14b) during the last two volume scans is consistent with increased centrifuging.

The  $Z_{\rm DR}$  profiles generally increase with height attaining a maximum between 1–1.5 km before decreasing at higher altitudes (Fig. 14d). Low  $Z_{\rm DR}$  occurs near the surface similar to the observations of  $\rho_{\rm hv}$ .

The  $Z_{\rm DR}$  profiles below 1.5 km also exhibit a similar clustering with the first four volume scans clustered between 1.5 to 2.0 dB at lower levels while the final four volumes are between 1.0 to 1.5 dB. There is a general trend for  $Z_{\rm DR}$  to decrease with time at lower levels. The profiles suggest a decrease in  $Z_{\rm DR}$  above 1.5 km for all volume scans. The decrease in  $Z_{\rm DR}$  with increasing debris loading is consistent with a reduced contribution of hydrometeors to the signal within the TDS. The strongest tornadic windspeeds are located near the surface as

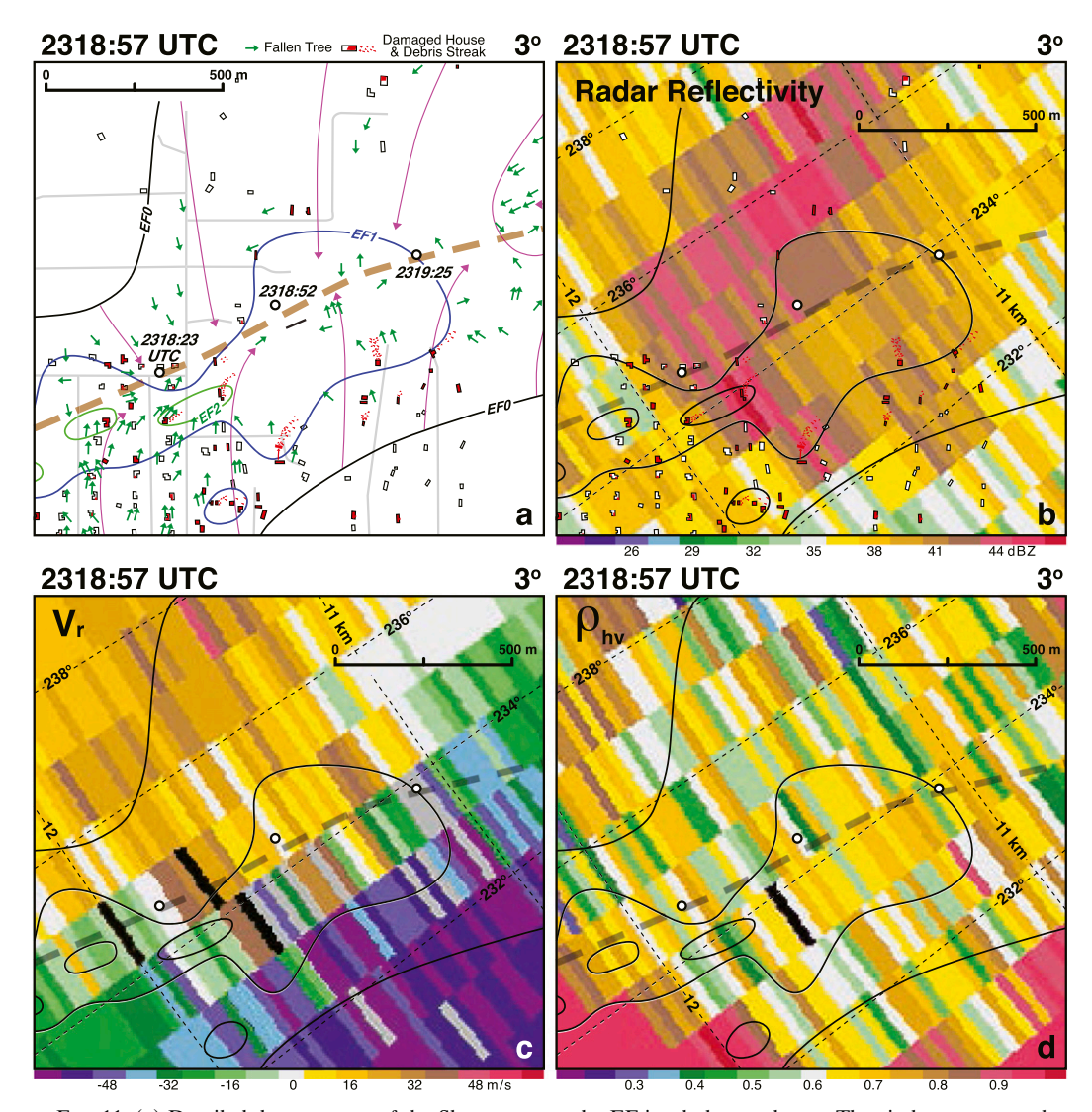


FIG. 11. (a) Detailed damage map of the Shawnee tornado. EF isopleths are drawn. The circles represent the location of the center of the rotational couplet at the indicated times. Dashed brown line denotes the center of the tornado track. Damaged and undamaged houses are distinguished by the white and red shading, respectively. Streaks of house debris are shown. Thin magenta lines represent the approximate direction of the flow based on debris streaks, fallen trees (green arrows), and striations marks in the fields. (b) Radar reflectivity scan at 3° from RaXPol at 2318:57 UTC. Damage analysis of the houses is also shown. (c) Doppler velocity scan at 3° from RaXPol at 2318:57 UTC. (d) Cross-correlation coefficient scan at 3° from RaXPol at 2318:57 UTC. Black pixels denote velocities that have been removed based on large spectral widths.

would be expected (Fig. 14b). The profiles of the Doppler velocity initially decrease in magnitude at the lowest levels as debris is lofted as noted earlier (cf. the 2316:10–2316:38 and 2316:42–2317:10 UTC profiles in Fig. 14b); however, the trend for each succeeding volume scan is for the velocity differential to increase between 0.5–2.5 km. Simulations of tornadoes suggest that azimuthal velocities are reduced when lofted debris is introduced (e.g., Lewellen et al. 2008; Bodine et al. 2016b). The profiles of velocity difference shown in Fig. 14b do not suggest that the tangential velocities

are decreasing as debris is lofted into the tornadic circulation. Instead, the speeds are increasing even after the ingestion of debris. The pattern of increasing velocity differential with greater debris lifting/loading in relationship with the TDS is noteworthy. For example, Bodine et al. (2013) speculated that tornado damage severity was related to the TDS characteristics. The present case shows this relationship with greater detail.

Bodine et al. (2013) proposed examining the 10th and 90th percentiles of  $\rho_{hv}$  and radar reflectivity,

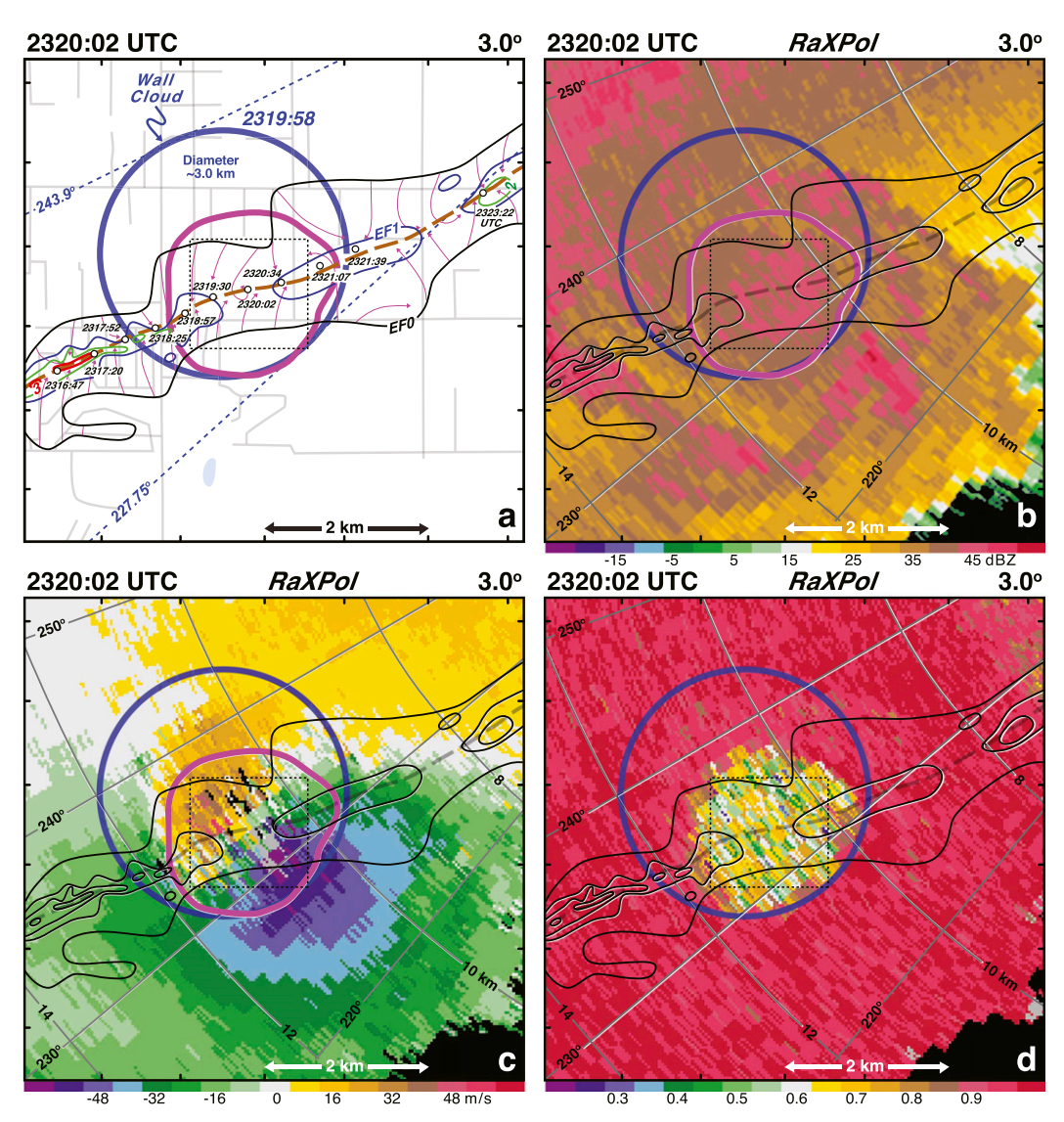


FIG. 12. (a) An enlargement of the Shawnee damage map. EF isopleths are drawn. The circles represent the location of the center of the rotational couplet at the indicated times. Dashed brown line denotes the center of the tornado track. Thin magenta lines represent the approximate direction of the flow based on debris streaks, fallen trees, and striation marks in the fields. Dashed blue lines are the azimuths from RaXPol. (b) Radar reflectivity scan, (c) Doppler velocity scan, and (d) cross-correlation coefficient scan at 3° from RaXPol at 2320:02 UTC. Thick magenta line in (a)–(c) and blue circle in (a)–(d) represent the approximate outline of the area of low  $\rho_{hv}$  and the wall cloud, respectively. Area shown in the figure is enclosed by the red box labeled "d" in Fig. 1. The dashed black box is enlarged in Fig. 13.

respectively, in order to understand the peak debris loading within tornadoes. The 90th percentile of radar reflectivity plots (Fig. 15a) are similar to the results shown in Fig. 14. There are low radar reflectivities near the surface and quasi-uniform intensity aloft that increases with time as more debris is lofted. The vertical profiles of the 90th percentile of  $\rho_{\rm hv}$  (Fig. 15b) provide a different perspective of the lofted debris than the areal averages presented in Fig. 14. The lowest two data points (2317:15–2318:16 UTC) have decreased

markedly when compared with the data collected during the earlier times. The  $\rho_{\rm hv}$  continues to fall at heights below 2 km during the next two volume scans (Fig. 15b) with the lowest values apparent at 2318:23–2318:48 UTC located between 0.5 and 2 km. The polarimetric data suggesting that there is an increase in lofted debris after 2316:45 UTC is consistent with the destruction of a number of structures shown in Figs. 5 and 7. Subsequently,  $\rho_{\rm hv}$  increases during the 2318:52–2319:20 UTC volume scan that continues until 2319:57–2320:26 UTC. The recovery of

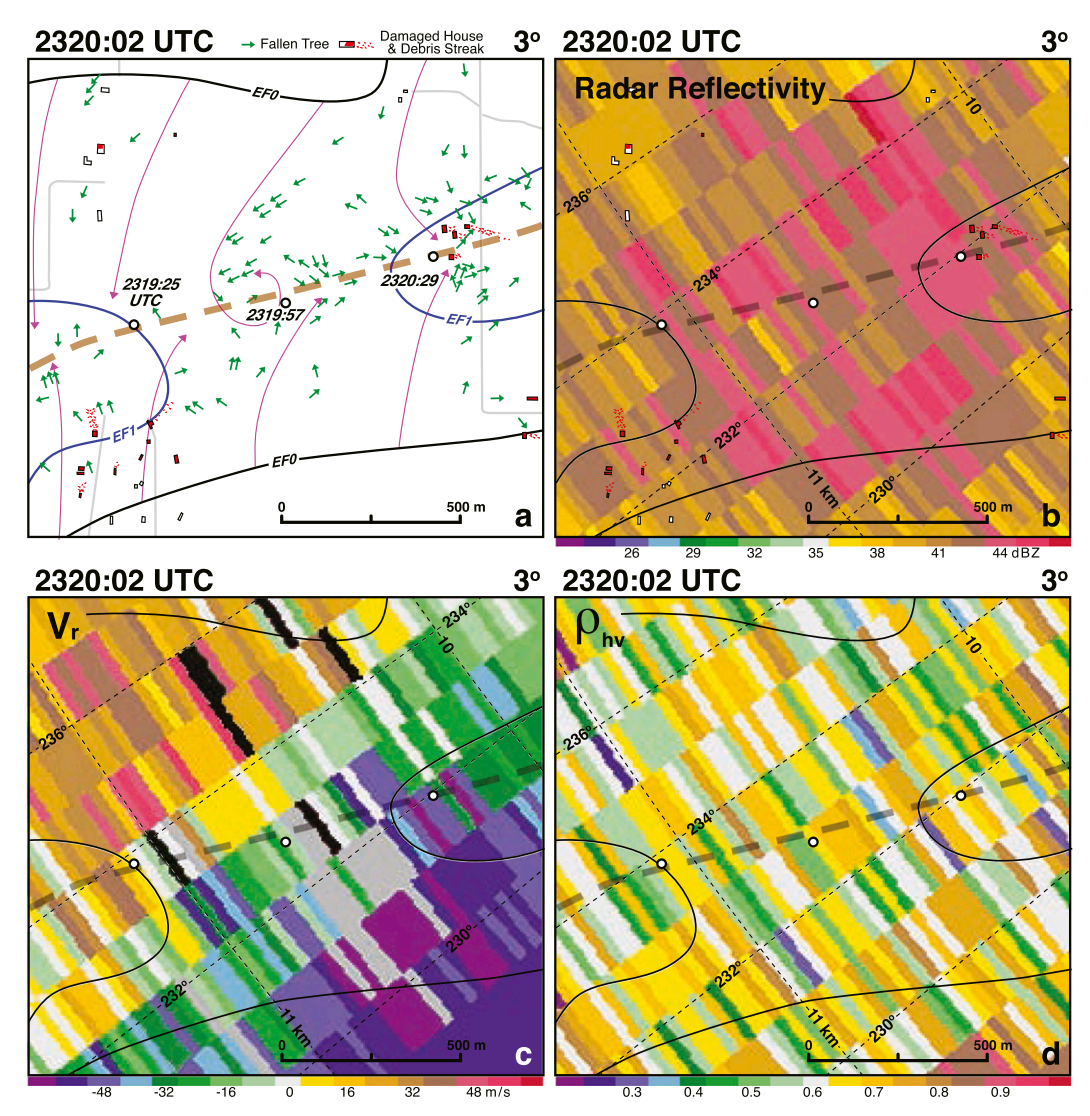


FIG. 13. (a) Detailed damage map of the Shawnee tornado. EF isopleths are drawn. The circles represent the location of the center of the rotational couplet at the indicated times. Dashed brown line denotes the center of the tornado track. Damaged and undamaged houses are distinguished by the white and red shading, respectively. Streaks of house debris are shown. Thin magenta lines represent the approximate direction of the flow based on debris streaks, fallen trees (green arrows), and striations marks in the fields. (b) Radar reflectivity scan at 3° from RaXPol at 2320:02 UTC. Damage analysis of the houses is also shown. (c) Doppler velocity scan at 3° from RaXPol at 2320:02 UTC. (d) Cross-correlation coefficient scan at 3° from RaXPol at 2320:02 UTC. Area in (a)–(d) is enclosed by the dashed black box shown in Fig. 12. Black pixels denote velocities that have been removed based on large spectral widths.

the 10th percentile of  $\rho_{\rm hv}$  to higher values, not noted in the mean  $\rho_{\rm hv}$  plots (Fig. 14), suggests that the largest debris had been centrifuged or fallen out whereas light debris remains or continues to be lofted over an area characterized by only a few scattered structures (e.g., Figs. 11 and 13).

Alternative explanations for the low  $\rho_{\rm hv}$  and high  $Z_{\rm DR}$  observations are presented in the following discussion. The relationship between debris size and/or concentration has been noted indirectly by several

past studies in which increases in radar reflectivity and decreases in  $\rho_{\rm hv}$  coincide with the increased damage at the surface and/or higher wind speeds implying greater amounts of lofted debris (Bodine et al. 2013, 2014; Van Den Broeke and Jauernic 2014; Wakimoto et al. 2018). Ryzhkov et al. (2005) noted that resonance scattering reduces  $\rho_{\rm hv}$  for larger scatterers compared to smaller scatterers. Therefore, both increased sizes or concentrations of debris should increase the relative concentration of debris to the backscattered signal and

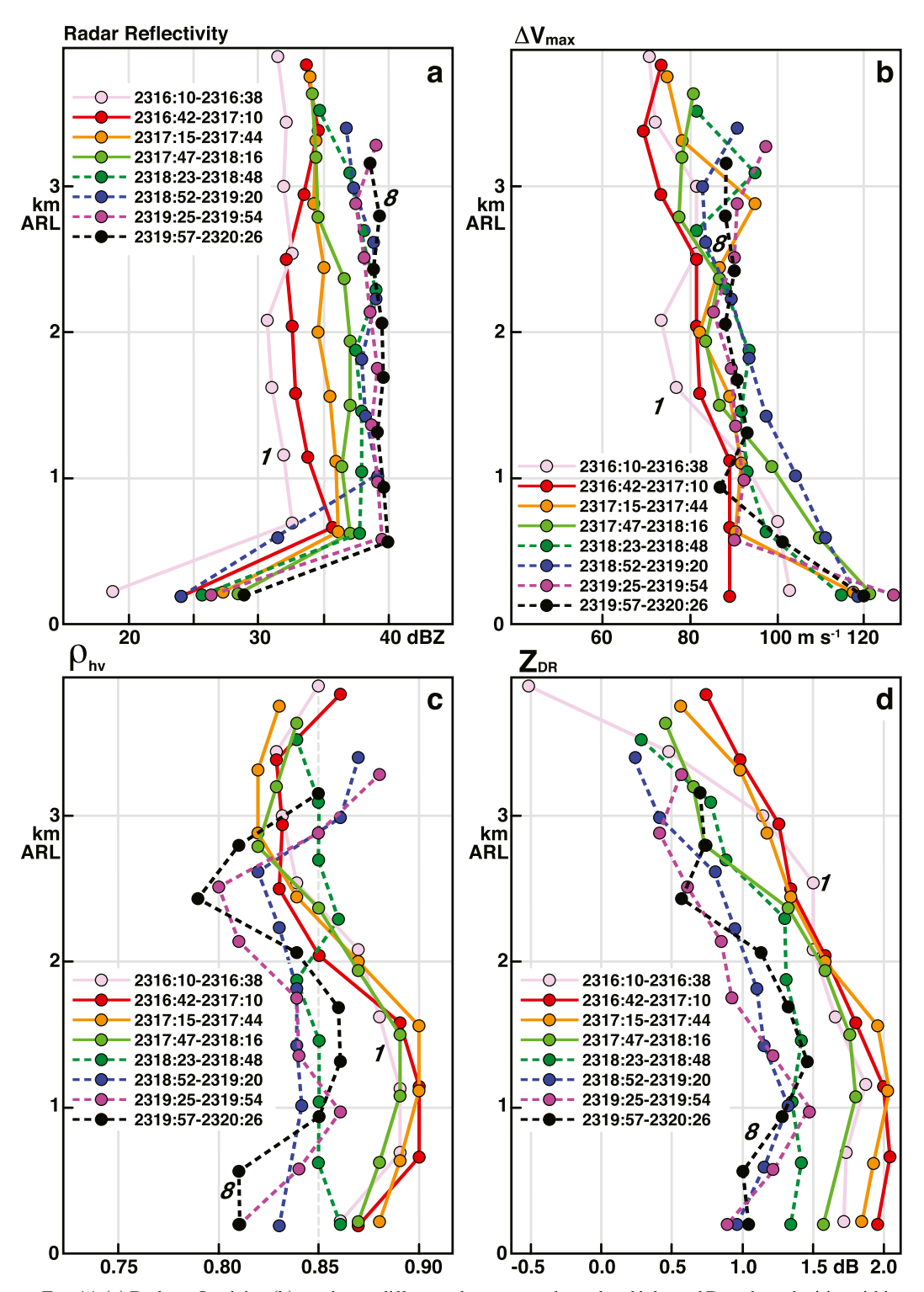


FIG. 14. (a) Radar reflectivity, (b) maximum difference between outbound and inbound Doppler velocities within the rotational couplet ( $\Delta V_{\rm max}$ ), (c) cross-correlation coefficient ( $\rho_{\rm hv}$ ), and (d) differential radar reflectivity ( $Z_{\rm DR}$ ) vs height above radar level (ARL). The variables shown in (a), (c), and (d) have been azimuthally averaged centered at the maximum vertical vorticity. Eight consecutive volumes scans collected by RaXPol are shown. The first (pink line) and last (black dashed line) volume scans are highlighted by the numbers 1 and 8 in the figures, respectively. The circles on each plot represent data collected at the radar elevation angles from 1° to 17° in 2° steps.

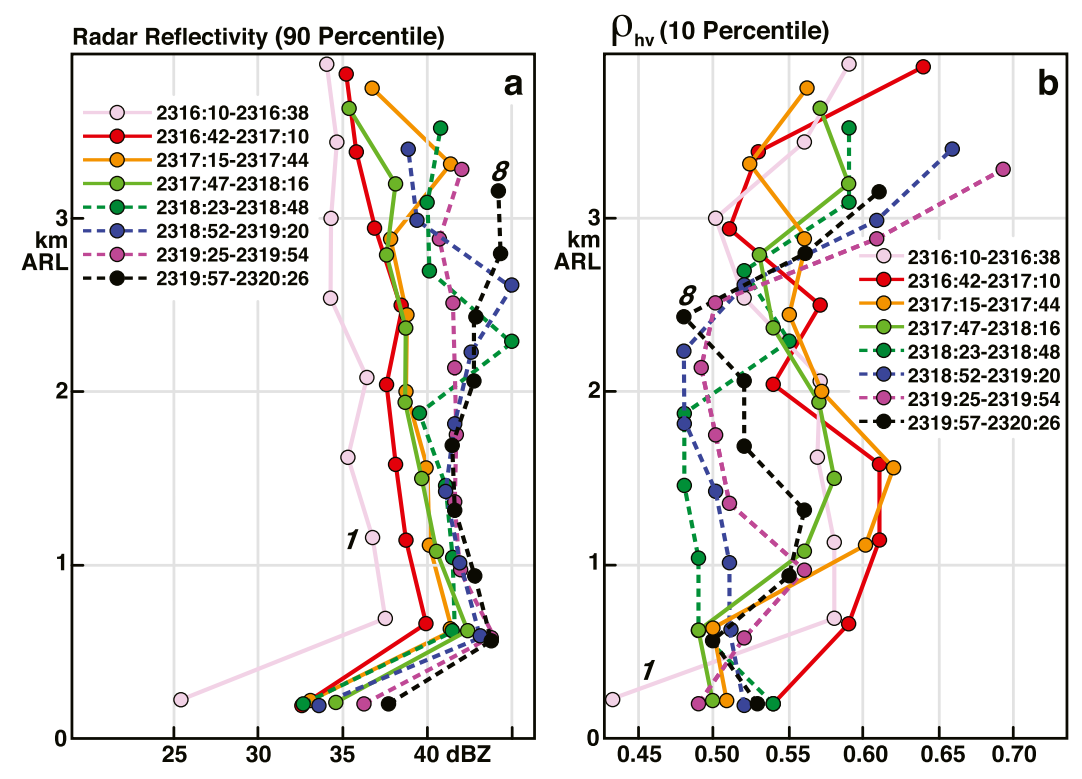


FIG. 15. (a) 90th percentile radar reflectivity and (b) 10th percentile cross-correlation coefficient ( $\rho_{hv}$ ) vs height above radar level (ARL). Eight consecutive volumes scans collected by RaXPol are shown. The first (pink line) and last (black dashed line) volume scans are highlighted by the numbers 1 and 8 in the figures, respectively. The circles on each plot represent data collected at the radar elevation angles from 1° to 17° in 2° steps.

thus reduce  $\rho_{\rm hv}$  (Bodine et al. 2016a). Radar reflectivity increases at low levels with time in Figs. 14 and 15 suggesting increasing sizes and/or concentration are consistent with these previous findings as well as the increase damage evident herein from the survey. Increasing diversity of shapes or orientations leading to a reduction in  $\rho_{\rm hv}$  is a possible alternative hypothesis. However, these factors alone cannot account for the increase in radar reflectivity. In addition, mean vertical profiles of  $Z_{\rm DR}$  within the TDS were calculated for the bottom 10% of  $\rho_{\rm hv}$  (not shown). These plots range from 0 to -1 dB but there is no systematic evolution that would suggest that debris orientation is becoming more chaotic.

It is possible that wetting of debris could lead to an increase in  $Z_{\rm DR}$  or a decrease in  $\rho_{\rm hv}$  rather than entrainment of precipitation into the TDS. However, the evidence from observations to date (Bluestein et al. 2007b; Bodine et al. 2011, 2014) suggest that wetting is secondary to the increased contribution of raindrops since  $\rho_{\rm hv}$  increases when significant amounts of precipitation are entrained. Support for this scenario is the decrease with time of the band of high radar reflectivity that coils up around the hook echo (not shown) suggesting

that less precipitation is being entrained in the TDS leading to the reduction in  $Z_{DR}$  (Fig. 14d).

### b. Dual-Doppler analysis

Dual-Doppler analyses using data collected by RaXPol and KTLX were possible at 2316:24 and 2319:39 UTC (Figs. 1e,f). The tornado produced damage rated EF3 at 2316:24 UTC (Fig. 16a). A detailed analysis of the damage and comparisons with radar reflectivity, single-Doppler velocity, and  $\rho_{hv}$  were shown in Figs. 6 and 7. The maximum vertical vorticity exceeds  $7 \times 10^{-2} \, \mathrm{s}^{-1}$  at 400 m and is centered along the tornado track in Fig. 16b. The radar reflectivity within the area encompassed by the strongest vertical vorticity is low since large amounts of debris have not yet been lofted to this height (Fig. 16b). Quasi-circular regions of low  $\rho_{hv}$  (Fig. 16c) and  $Z_{DR}$ (Fig. 16d) outline the areas of lofted debris that are probably comprised of small particles based on the relatively low radar reflectivity. The TDS is positioned within an area characterized by convergence with a minimum ( $<-30 \times 10^{-3} \,\mathrm{s}^{-1}$ ) located on the western and northern edge of the TDS (Fig. 16c). Strong tornado-relative winds are located north of the TDS and also within the band of high  $Z_{DR}$  advecting

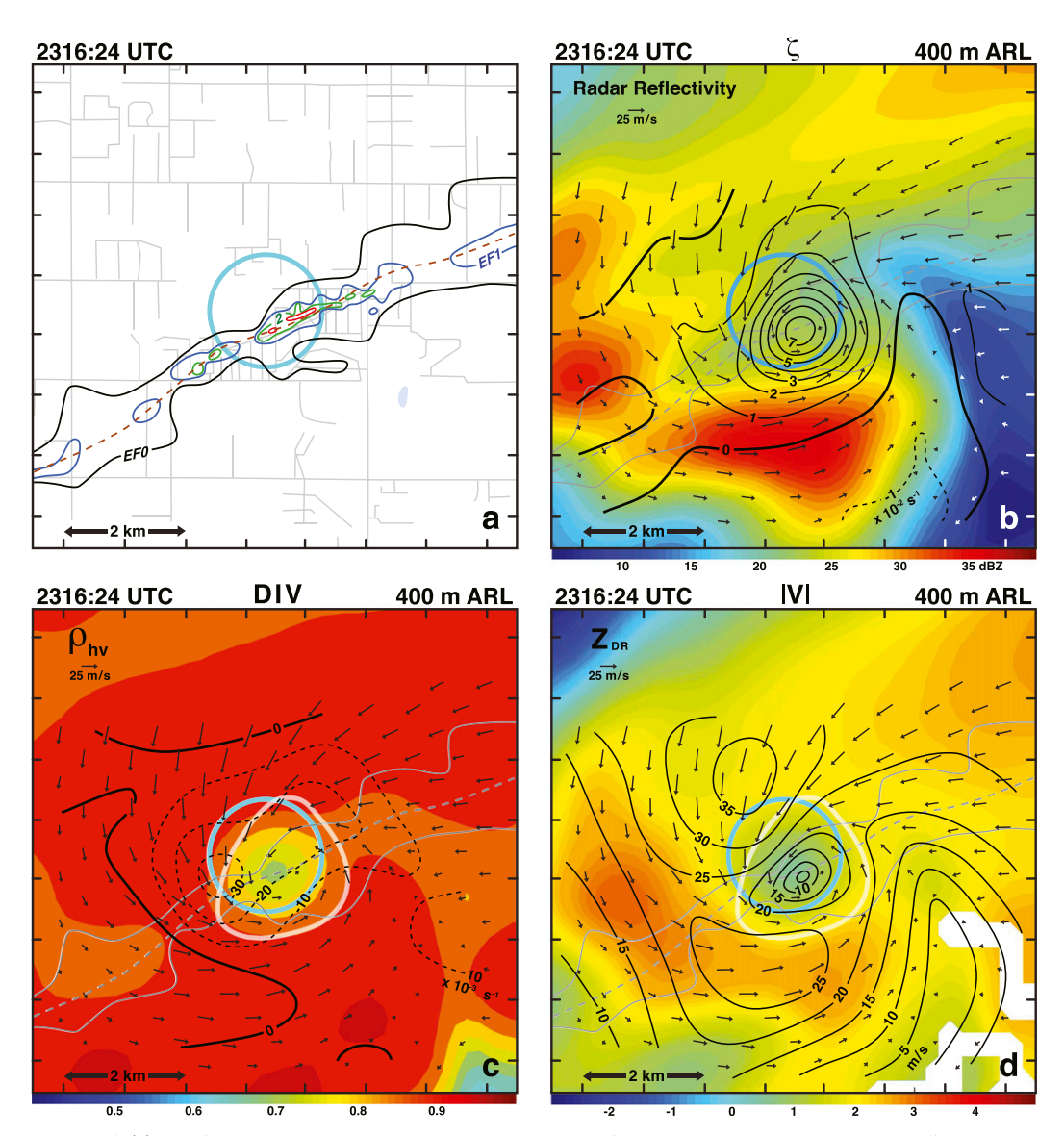


FIG. 16. (a) Detailed damage map of the Shawnee tornado. EF isopleths are drawn. Dashed brown line denotes the center of the tornado track. (b) Interpolated radar reflectivity at 400 m above radar level (ARL) from RaXPol at 2316:24 UTC. Vertical vorticity analysis based on dual-Doppler wind synthesis is shown. (c) Cross-correlation coefficient ( $\rho_{\rm hv}$ ) at 400 m ARL from RaXPol at 2316:24 UTC. Horizontal divergence analysis based on a dual-Doppler wind synthesis is shown. (d) Differential reflectivity ( $Z_{\rm DR}$ ) at 400 m ARL from RaXPol at 2316:24 UTC. Magnitude of the tornado-relative wind speed based on dual-Doppler wind synthesis is shown. Blue circle plotted in (a)–(d) is the approximate location of the wall cloud. White line in (c) and (d) is the  $2\times10^{-2}\,{\rm s}^{-1}$  isopleth of vertical vorticity. The solid and dashed gray lines in (b)–(d) are the EF0 isopleth and location of the center of the tornado track, respectively. The tornado-relative wind vectors are plotted in (b)–(d). Location of the analysis depicted in this figure is shown by the green box labeled "e" in Fig. 1.

hydrometeors around the southern flank of the TDS (Fig. 16d).

The tornado was producing damage rated EF0 (Fig. 13) during the next volume scan at 2319:39 UTC (Fig. 17). The radar reflectivity near the tornado has increased as a result of lofted debris but stronger echoes in other regions surrounding the hook echo are the result of

increased number of raindrops (e.g., large, positive  $Z_{\rm DR}$  north and west of the TDS suggests an increase in the size of the raindrops in that region). The vertical vorticity associated with the tornadic circulation has increased (>10 × 10<sup>-2</sup> s<sup>-1</sup>) resulting from the stronger windspeeds swirling around the center of the circulation (Figs. 14b and 17d). The increased lofted debris has not

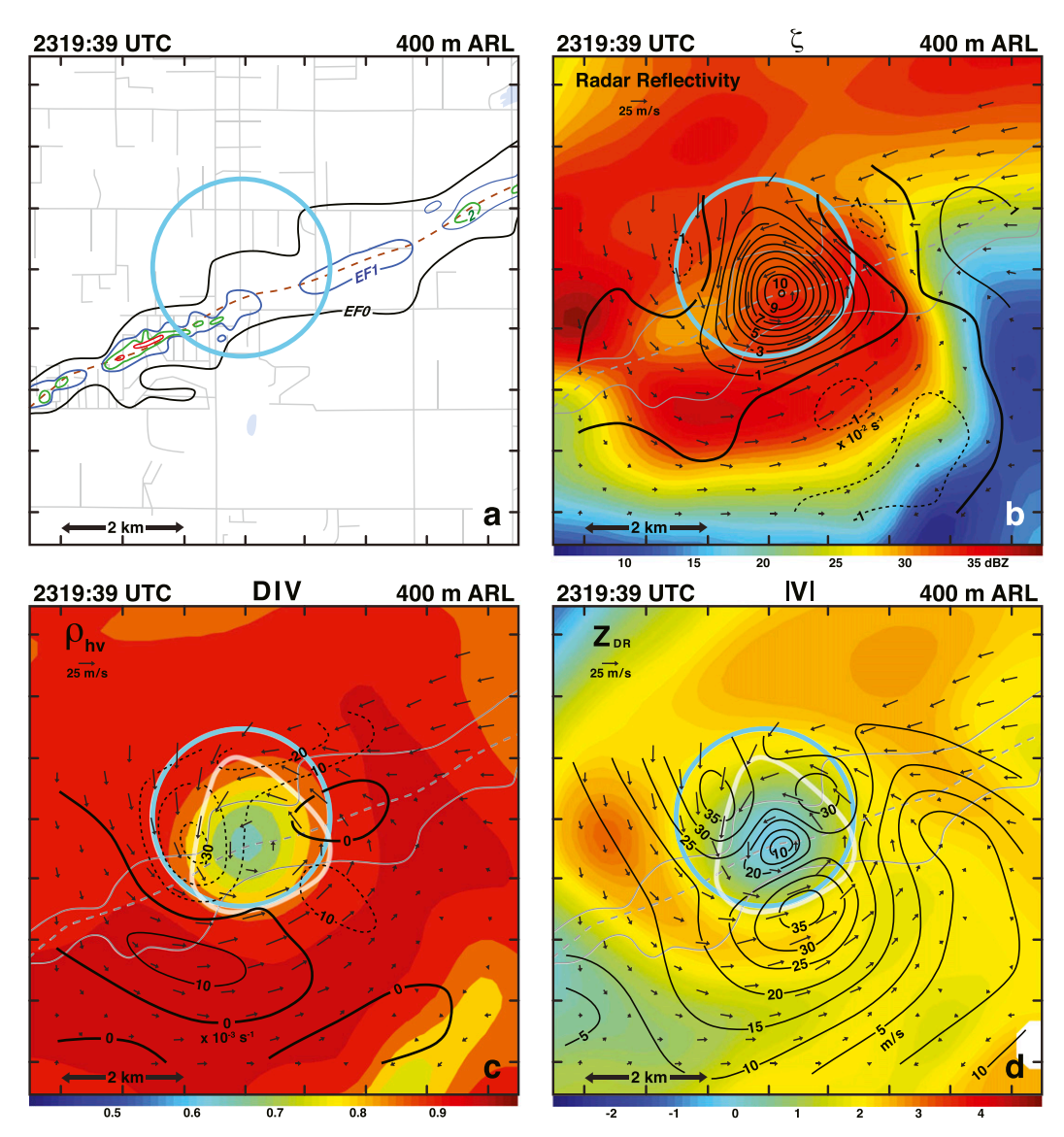


FIG. 17. (a) Detailed damage map of the Shawnee tornado. EF isopleths are drawn. Dashed brown line denotes the center of the tornado track. (b) Interpolated radar reflectivity at 400 m above radar level (ARL) from RaXPol at 2319:39 UTC. Vertical vorticity analysis based on dual-Doppler wind synthesis is shown. (c) Cross-correlation coefficient ( $\rho_{\rm hv}$ ) at 400 m ARL from RaXPol at 2319:39 UTC. Horizontal divergence analysis based on a dual-Doppler wind synthesis is shown. (d) Differential reflectivity ( $Z_{\rm DR}$ ) at 400 m ARL from RaXPol at 2319:39 UTC. Magnitude of the tornado-relative wind speed based on dual-Doppler wind synthesis is shown. Blue circle plotted in (a)–(d) is the approximate location of the wall cloud. White line in (c) and (d) is the  $2\times10^{-2}\,{\rm s}^{-1}$  isopleth of vertical vorticity. The solid and dashed gray lines in (b)–(d) are the EF0 isopleth and location of the center of the tornado track, respectively. The tornado-relative wind vectors are plotted in (b)–(d). Location of the analysis depicted in this figure is shown by the green box labeled "f" in Fig. 1.

resulted in a reduction in tangential velocities or vertical vorticity. The TDS has increased in areal extent and the minimum  $\rho_{\rm hv}$  and  $Z_{\rm DR}$  within the TDS have fallen compared to the earlier analyses (Figs. 17c,d) in response to the increased amount of debris. The TDS is still characterized by convergent flow although it is weaker east and south of the tornado. It is possible that

the increase in lofted debris has resulted in positive bias in the tornado-relative radial velocity and an increase in the apparent divergent flow in these regions. The divergent flow south of the TDS (Fig. 17c) is associated with an intrusion of low  $Z_{\rm DR}$ . French et al. (2015) proposed that the low  $Z_{\rm DR}$  in this region was a result of smaller raindrops within a dynamically driven downdraft.

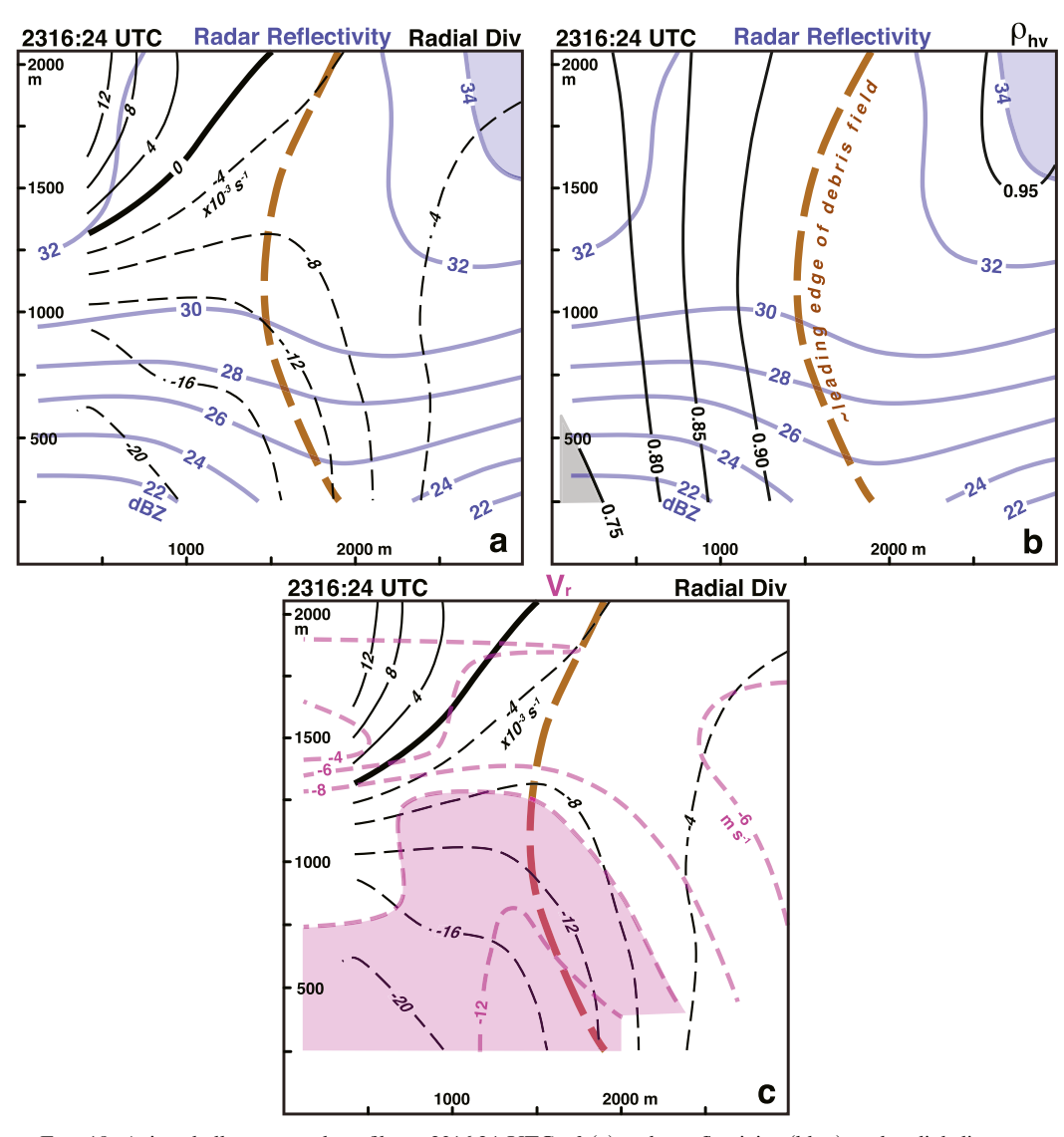


FIG. 18. Azimuthally averaged profile at 2316:24 UTC of (a) radar reflectivity (blue) and radial divergence (black), (b) radar reflectivity (blue) and cross-correlation coefficient ( $\rho_{hv}$ , black), and (c) tornado-relative radial velocities (magenta) and radial component of divergence (black). Brown-dashed line denotes the leading edge of the debris field based on the gradient of  $\rho_{hv}$ . Radar reflectivity shaded light blue are >34 dBZ.  $\rho_{hv}$  less than 0.75 is shaded gray. Radial velocities shaded light magenta are less than -10 m s<sup>-1</sup>. Solid and dashed black lines in (a) and (c) represent divergence and convergence, respectively. The distance from the tornado's axis is plotted on the abscissa. The ordinate is height above radar level (ARL).

The results presented in the figure are consistent with that finding.

The vertical structure of the lofted debris based on azimuthally averaged profiles centered on the tornado for the dual-Doppler analyses times is shown (Figs. 18 and 19). The tornado was in the early stages of causing damage at the surface rated EF2–EF3 at 2316:24 UTC. The radar reflectivity is low near the surface and increases with height (Figs. 18a,b). Beam blockage is contributing to the reduced reflectivities near the surface. It is also possible that the higher radar reflectivity

near the surface may not be resolved owing to the beam height. The weak echo hole (WEH) is not being resolved in the profile. The brown-dashed line that denotes the leading edge of the debris field is based on an analysis of the horizontal gradient at 0.01 intervals (not shown) of  $\rho_{\rm hv}$ . The minimum in  $\rho_{\rm hv}$  is near the tornado center and close to the ground where large amounts of lofted debris are located (Fig. 18b). The leading edge of the lofted debris is close to the ridge of high radar reflectivity at low levels (Figs. 18a,b). The area shown in Fig. 18a is characterized by convergence except above 1.5 km and

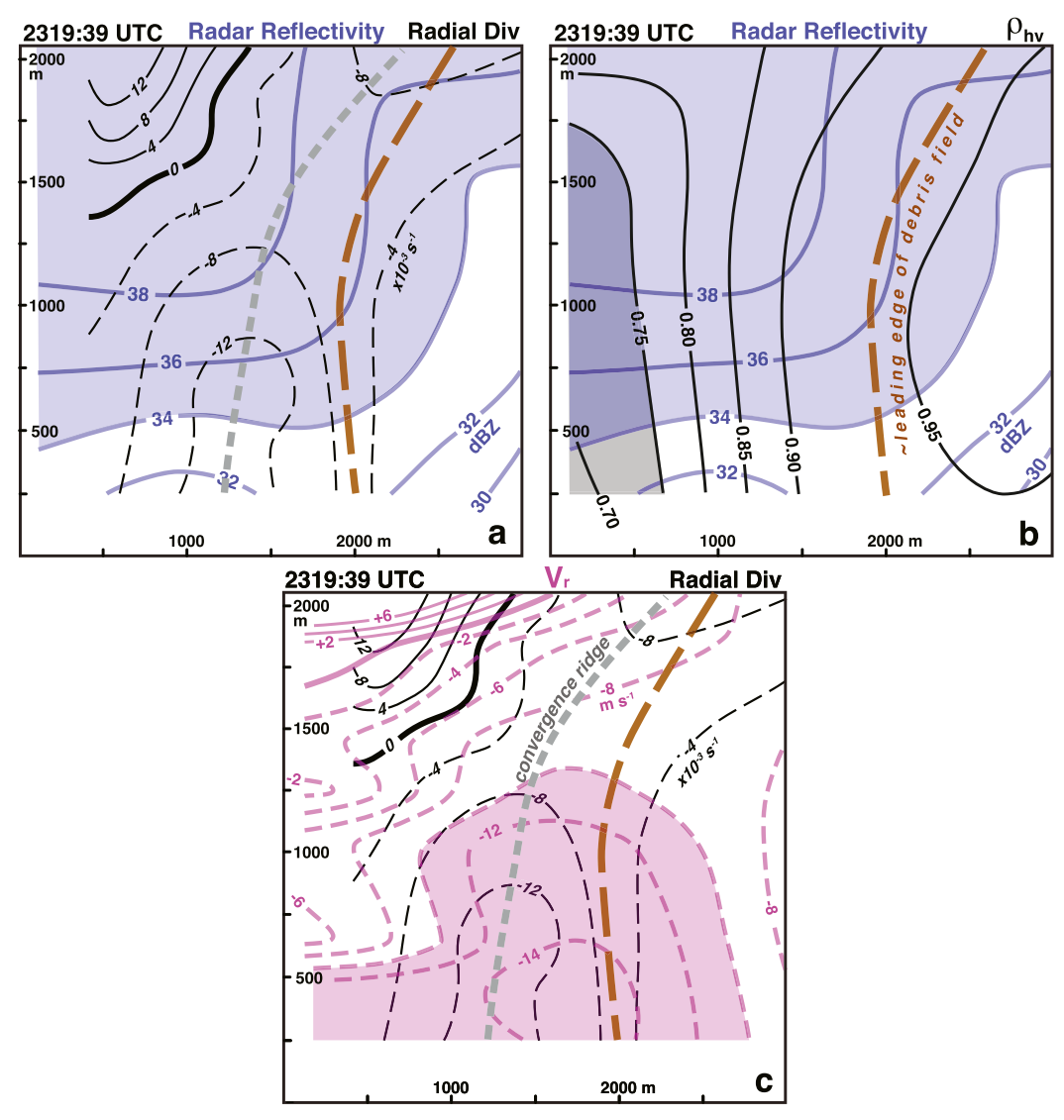


FIG. 19. Azimuthally averaged profile at 2319:39 UTC of (a) radar reflectivity (blue) and radial divergence (black), (b) radar reflectivity (blue) and cross-correlation coefficient ( $\rho_{hv}$ , black), and (c) tornado-relative radial velocities (magenta) and radial component of divergence (black). Brown-dashed line denotes the leading edge of the debris field based on the gradient of  $\rho_{hv}$ . Dashed gray line denotes the location of a convergence ridge. Radar reflectivity shaded light blue are >34 dBZ and  $\rho_{hv}$  less than 0.75 is shaded gray. Radial velocities shaded light magenta are less than  $-10 \, \mathrm{m \, s}^{-1}$ . Solid and dashed black lines in (a) and (c) represent divergence and convergence, respectively. The distance from the tornado's axis is plotted on the abscissa. The ordinate is height above radar level (ARL).

near the tornado axis. The low-level convergence illustrated in the figure should not be assumed to represent the much smaller-scale confluence patterns in the debris. Inflow into the tornado is encountering lofted debris particles that would bias the Doppler velocities with a positive component of tornado-relative radial motion owing to centrifuging. The bias is hypothesized to be the contributing to the convergence observed in the Doppler velocity analysis. The convergence increased close to the tornado axis.

Large amounts of lofted debris from the damaged structures rated EF3 (Fig. 5) have been ingested into the tornadic circulation and are apparent by the increase in radar reflectivity (Figs. 19a,c) and a reduction in  $\rho_{\rm hv}$  (Fig. 19b). The leading edges of the lofted debris (dashed brown line) and large radar reflectivities (area shaded blue) are nearly coincident as might be expected (Fig. 19). The former is positioned at a larger radius compared to the previous analysis time. A ridge of maximum convergence is apparent between 1–2 km

from the tornado axis and near the leading edge of the debris field. The appearance of this convergence zone during the time when significant debris has been lofted suggests that increased debris centrifuging may be contributing to its formation. Centrifuging would increase the positive bias in the tornado-relative radial velocity and, therefore, the convergence near the leading edge of the debris field. The ring of convergence has been shown before by Wakimoto et al. (2016) although its position was slightly beyond the TDS. The different locations of the convergence ring could be related to the type of debris that is lofted. This is the first time that the vertical structure of the convergence zone has been shown. The ridge of convergence in the zone closely matches the slope of the leading edge of the debris field (Fig. 19c), which provides additional evidence that its existence is attributable to centrifuged debris. The decrease in convergence close to the tornado axis (<1 km) at lower levels (cf. Figs. 18a and 19a) is most likely a result of the increasing effect of debris centrifuging (i.e., an increase in the positive bias in the tornado-relative radial velocity producing an anomalous divergent signature).

### 5. Discussion and summary

An aerial and ground survey was combined with highresolution mobile, rapid-scanning X-band polarimetric radar data collected on a tornado near Shawnee, Oklahoma. Indeed, rapid scan polarimetric data are needed to characterize the debris field evolution since large debris fall out faster due to larger terminal velocities. The observational period encompassed a time when the tornado was producing damage rated EF3. This is believed to be the first time a detailed aerial mapping of intense damage to structures and trees has been compared with mobile polarimetric data. Previous studies by Wakimoto et al. (2015, 2016, and 2018) did not present analyses of polarimetric data when numerous structures were destroyed and large amounts of debris were suddenly lofted in the tornado. A detailed study of structural damage caused by a tornado was presented by Atkins et al. (2014) but the spatial and temporal resolution of the polarimetric data recorded by the WSR-88D radar were relatively coarse compared to RaXPol data presented in the current study.

The radar reflectivity increased as large amounts of debris were lofted. In addition, there was a drop in  $\rho_{\rm hv}$  and  $Z_{\rm DR}$  as well as an increase in the areal extent of the TDS. The Doppler velocity differential accompanying the tornado at low levels initially decreased as more debris became airborne. Subsequently, the velocity differential increased with time, which is contrary to results shown in numerical simulations of lofted debris.

Accordingly, either the amount of debris was not sufficient to reduce the wind speeds of the tornado or that storm/tornado-scale processes that increased the tornado's intensity had a greater influence than any changes caused by debris loading.

Fortunately, dual-Doppler analyses were performed at two times by combining data collected by RaXPol and KTLX WSR-88D. The tornado was in the early stages of creating intense damage to structures rated EF3 at the initial analysis time. Large debris particles were lofted by the tornado to higher levels during the second time period. Azimuthally averaged profiles centered on the tornado axis were created to analyze the debris field and its potential impact on the low-level convergence. An increase in radar reflectivity after large amounts of debris were lofted was apparent. It is hypothesized that low-level inflow into the tornado would experience a positive bias in the tornado-relative radial velocities upon entering the debris cloud. The Doppler radar wind syntheses would resolve a false decrease in radial inflow that would lead to an increase in radial convergence. A ridge of radial convergence was noted to the rear of the leading edge of debris. The vertical structure of this convergence zone was shown for the first time and its slope closely matched the slope of the leading edge of the debris field providing additional evidence that its existence was a result of debris centrifuging.

A schematic model summarizing observations during a period when large amounts of debris were lofted is presented in Fig. 20. The isopleths of radar reflectivity and radial convergence in relation to the debris field are shown. Dashed blue lines denote the location of the WEH, which was not resolved in the dual-Doppler profiles. Images of trees on the figure depict the impact of beam blockage on the radar reflectivity. The blue arrows are the tornado-relative horizontal winds. The positive bias in the tornado-relative radial velocity once the inflow enters the debris cloud is shown by both the reduction in inflow speeds and an increase in radial convergence. The ring of maximum in radial convergence within the debris cloud is also shown (highlighted by the white dashed line).

Mobile, polarimetric radars have increased our understanding of both the wind and swirling debris fields that accompany tornadoes. The current study helps to delineate the effect of lofted debris on the radial velocities recorded by a Doppler radar. It also provides another example that tornadoes that are laden with debris may not experience a sustained reduction in windspeeds. Documenting the evolution of the lofted debris field at high temporal resolution with dual-polarization radars combined with detailed damage surveys are needed owing to the rapid changes that are occurring within the tornado.

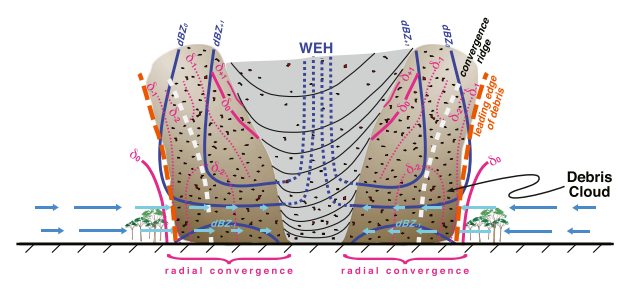


FIG. 20. Schematic model of debris lofted by the tornado. Blue arrows represent the tornado-relative horizontal winds. Approximate radar reflectivity and radial convergence profiles are represented by the blue and magenta lines, respectively. Dashed blue lines represents the isopleths of radar reflectivity that define the weak echo hole (WEH) that were not resolved in the profiles shown in this study. White dashed lines represent the region of maximum convergence. Brown dashed lines represent the leading edit of the lofted debris. Blockage of the radar beam by trees is illustrated.

Acknowledgments. Zach Wienhoff and Howard Bluestein were supported by NSF Grants AGS-1262048 and 1560945. David Bodine was supported by NSF AGS-1823478. NSF MRI Grant AGS-0821231 supported the development of RaXPol. The authors acknowledge the support from Jana Houser and Vivek Mahale with the RaXPol deployment on this day. Kelly Butler helped the lead author with the photographic documentation of the tornado. The authors also wish to acknowledge John Meier, Tian Yu, and Bob Palmer at the Advanced Radar Research Center (ARRC) for maintaining RaXPol. The comments from two anonymous reviewers and Dave Lewellen significantly improved an earlier version of the manuscript.

### REFERENCES

- Adlerman, E. J., and K. K. Droegemeier, 2005: The dependence of numerically simulated cyclic mesocyclogenesis upon environmental vertical wind shear. *Mon. Wea. Rev.*, 133, 3595– 3623, https://doi.org/10.1175/MWR3039.1.
- Atkins, N. T., K. M. Butler, K. R. Flynn, and R. M. Wakimoto, 2014: An integrated damage, visual, and radar analysis of the 2013 Moore, Oklahoma, EF5 tornado. *Bull. Amer. Meteor. Soc.*, 95, 1549–1561, https://doi.org/10.1175/BAMS-D-14-00033.1.
- Barnes, S. L., 1964: A technique for maximizing details in numerical weather map analysis. *J. Appl. Meteor.*, **3**, 396–409, https://doi.org/10.1175/1520-0450(1964)003<0396:ATFMDI>2.0.CO;2.
- Bluestein, H. B., C. C. Weiss, and A. L. Pazmany, 2004: The vertical structure of a tornado near Happy, Texas, on 5 May 2002: High-resolution, mobile, W-band, Doppler radar observations. Mon. Wea. Rev., 132, 2325–2337, https://doi.org/10.1175/ 1520-0493(2004)132<2325:TVSOAT>2.0.CO;2.
- —, M. M. French, E. M. Holthaus, and R. L. Tanamachi, 2007a: The structure of tornadoes near Attica, Kansas, on 12 May 2004: High-resolution, mobile, Doppler radar observations. *Mon. Wea. Rev.*, **135**, 475–506, https://doi.org/10.1175/MWR3295.1.

- —, M. M. French, R. L. Tanamachi, S. Frasier, K. Hardwick, F. Junyent, and A. L. Pazmany, 2007b: Close-range observations of tornadoes in supercells made with dual-polarization, X-band, mobile, Doppler radar. *Mon. Wea. Rev.*, 135, 1522–1543, https://doi.org/10.1175/MWR3349.1.
- —, J. C. Snyder, and J. B. Houser, 2015: A multiscale overview of the El Reno, Oklahoma, tornadic supercell of 31 May 2013. Wea. Forecasting, 30, 525–552, https://doi.org/10.1175/WAF-D-14-00152.1.
- —, K. J. Thiem, J. C. Snyder, and J. B. Houser, 2018: The multiple-vortex structure of the El Reno, Oklahoma, tornado on 31 May 2013. *Mon. Wea. Rev.*, **146**, 2483–2502, https:// doi.org/10.1175/MWR-D-18-0073.1.
- ——, ——, and ——, 2019: Tornadogenesis and early tornado evolution in the El Reno, Oklahoma, supercell on 31 May 2013. *Mon. Wea. Rev.*, **147**, 2045–2066, https://doi.org/10.1175/MWR-D-18-0338.1.
- Bodine, D. J., M. R. Kumjian, A. J. Smith, R. D. Palmer, A. V. Ryzhkov, and P. L. Heinselman, 2011: High-resolution polarimetric observations of an EF4 tornado on 10 May 2010 from OU-PRIME. 35th Conf. on Radar Meteorology, Pittsburg, PA, Amer. Meteor. Soc., 4B3, https://ams.confex.com/ams/35Radar/webprogram/Paper191661.html.
- —, —, R. D. Palmer, P. L. Heinselman, and A. V. Ryzhkov, 2013: Tornado damage estimation using polarimetric radar. Wea. Forecasting, 28, 139–158, https://doi.org/10.1175/WAF-D-11-00158.1.
- ——, R. D. Palmer, and G. Zhang, 2014: Dual-wavelength polarimetric radar analyses of tornadic debris signatures. *J. Appl. Meteor. Climatol.*, **53**, 242–261, https://doi.org/10.1175/JAMC-D-13-0189.1.
- —, T. Maruyama, C. J. Fulton, Y. Zhu, and B. L. Cheong, 2016a: Simulated frequency dependence of radar observations of tornadoes. *J. Atmos. Oceanic Technol.*, 33, 1825–1842, https://doi.org/10.1175/JTECH-D-15-0120.1.
- —, T. Maruyama, R. D. Palmer, C. J. Fulton, H. B. Bluestein, and D. C. Lewellen, 2016b: Sensitivity of tornado dynamics to soil debris loading. *J. Atmos. Sci.*, 73, 2783–2801, https://doi.org/10.1175/JAS-D-15-0188.1.
- Burgess, D. W., V. T. Wood, and R. A. Brown, 1982: Mesocyclone evolution statistics. Preprints, 12th Conf. on Severe Local Storms, San Antonio, TX, Amer. Meteor. Soc., 422–424.
- Cheong, B. L., D. J. Bodine, C. J. Fulton, S. M. Torres, T. Maruyama, and R. D. Palmer, 2017: SimRadar: A polarimetric radar time series simulator for tornadic debris studies. *IEEE Trans. Geosci. Remote Sens.*, 55, 2858–2870, https://doi.org/10.1109/TGRS.2017.2655363.
- Doswell, C. A., and H. E. Brooks, 2002: Lessons learned from the damage produced by the tornadoes of 3 May 1999. *Wea. Forecasting*, **17**, 611–618, https://doi.org/10.1175/1520-0434(2002)017<0611:LLFTDP>2.0.CO;2.
- Dowell, D. C., and H. B. Bluestein, 2002: The 8 June 1995 McLean, Texas, storm. Part I: Observations of cyclic tornadogenesis. *Mon. Wea. Rev.*, **130**, 2626–2648, https://doi.org/10.1175/1520-0493(2002)130<2626:TJMTSP>2.0.CO;2.
- —, C. R. Alexander, J. M. Wurman, and L. J. Wicker, 2005: Centrifuging of hydrometeors and debris in tornadoes: Radar-reflectivity patterns and wind-measurement errors. *Mon. Wea. Rev.*, 133, 1501–1524, https://doi.org/10.1175/ MWR2934.1.
- French, M. M., D. W. Burgess, E. R. Mansell, and L. J. Wicker, 2015: Bulk hook echo raindrop sizes retrieved using mobile, polarimetric Doppler radar observations. J. Appl. Meteor.

- Climatol., 54, 423–450, https://doi.org/10.1175/JAMC-D-14-0171.1.
- Fujita, T. T., 1974: Jumbo tornado outbreak of 3 April 1974. Weatherwise, 27, 116–126, https://doi.org/10.1080/00431672.1974.9931693.
- Giangrande, S. E., 2002: Investigation of polarimetric measurements of rainfall at close and distant ranges. M.S. thesis, School of Meteorology, University of Oklahoma, 86 pp.
- Hildebrand, P. H., and R. K. Moore, 1990: Meteorological radar observations from mobile platforms. *Radar in Meteorology*, D. Atlas, Ed., Amer. Meteor. Soc., 287–314.
- Houser, J. L., H. B. Bluestein, and J. C. Snyder, 2015: Rapid-scan, polarimetric, Doppler radar observations of tornadogenesis and tornado dissipation in a tornadic supercell: The "El Reno, Oklahoma" storm of 24 May 2011. *Mon. Wea. Rev.*, 143, 2685–2710, https://doi.org/10.1175/MWR-D-14-00253.1.
- —, —, and —, 2016: A finescale radar examination of the tornadic debris signature and weak-echo reflectivity band associated with a large, violent tornado. *Mon. Wea. Rev.*, **144**, 4101–4130, https://doi.org/10.1175/MWR-D-15-0408.1.
- Isom, B., and Coauthors, 2013: The atmospheric imaging radar: Simultaneous volumetric observations using a phased array weather radar. *J. Atmos. Oceanic Technol.*, **30**, 655–675, https://doi.org/10.1175/JTECH-D-12-00063.1.
- Kosiba, K., and J. Wurman, 2010: The three-dimensional axisymmetric wind field structure of the Spencer, South Dakota, 1998 tornado. J. Atmos. Sci., 67, 3074–3083, https://doi.org/10.1175/2010JAS3416.1.
- Kumjian, M. R., and A. V. Ryzhkov, 2008: Polarimetric signatures in supercell thunderstorms. J. Appl. Meteor. Climatol., 47, 1940–1961, https://doi.org/10.1175/2007JAMC1874.1.
- Kurdzo, J. M., D. J. Bodine, B. L. Cheong, and R. D. Palmer, 2015: High-temporal resolution polarimetric X-band Doppler radar observations of the 20 May 2013 Moore, Oklahoma, tornado. *Mon. Wea. Rev.*, 143, 2711–2735, https://doi.org/10.1175/MWR-D-14-00357.1.
- ——, and Coauthors, 2017: Observations of severe local storms and tornadoes with the atmospheric imaging radar. *Bull. Amer. Meteor. Soc.*, **98**, 915–935, https://doi.org/10.1175/BAMS-D-15-00266.1.
- Lee, W.-C., and J. Wurman, 2005: Diagnosed three-dimensional axisymmetric structure of the Mulhall tornado on 3 May 1999. J. Atmos. Sci., 62, 2373–2393, https://doi.org/10.1175/ JAS3489.1.
- Lewellen, D. C., and M. I. Zimmerman, 2008: Using simulated tornado surface marks to help decipher near-ground wind fields. 24th Conf. on Severe Local Storms, Savannah, GA, Amer. Meteor. Soc., 8B1, https://ams.confex.com/ams/24SLS/ techprogram/paper\_141749.htm.
- ——, B. Gong, and W. S. Lewellen, 2008: Effects of finescale debris on near-surface tornado dynamics. *J. Atmos. Sci.*, **65**, 3247–3262, https://doi.org/10.1175/2008JAS2686.1.
- Mahre, A., J. M. Kurdzo, D. J. Bodine, C. B. Griffen, R. D. Palmer, and T.-Y. Yu, 2018: Analysis of the 16 May 2015 Tipton, Oklahoma, EF-3 tornado at high spatiotemporal resolution using the atmospheric imaging radar. *Mon. Wea. Rev.*, 146, 2103–2124, https://doi.org/10.1175/MWR-D-17-0256.1.
- Majcen, M., P. Markowski, Y. Richardson, D. Dowell, and J. Wurman, 2008: Multipass objective analyses of Doppler radar data. J. Atmos. Oceanic Technol., 25, 1845–1858, https:// doi.org/10.1175/2008JTECHA1089.1.
- Malkus, J., 1952: The slopes of cumulus clouds in relation to external wind shear. *Quart. J. Roy. Meteor. Soc.*, **78**, 530–542, https://doi.org/10.1002/qj.49707833804.

- Nolan, D. S., 2013: On the use of Doppler radar-derived wind fields to diagnose the secondary circulations of tornadoes. *J. Atmos. Sci.*, 70, 1160–1171, https://doi.org/10.1175/JAS-D-12-0200.1.
- Pauley, P. M., and X. Wu, 1990: The theoretical, discrete, and actual response of the Barnes objective analysis scheme for one- and two-dimensional fields. *Mon. Wea. Rev.*, 118, 1145–1164, https://doi.org/10.1175/1520-0493(1990)118<1145: TTDAAR>2.0.CO:2.
- Pazmany, A. L., J. B. Mead, H. B. Bluestein, J. C. Snyder, and J. B. Houser, 2013: A mobile rapid-scanning X-band polarimetric (RaXPol) Doppler radar system. J. Atmos. Oceanic Technol., 30, 1398–1413, https://doi.org/10.1175/JTECH-D-12-00166.1.
- Ryzhkov, A., D. Burgess, D. Zrnić, T. Smith, and S. Giangrande, 2002: Polarimetric analysis of a 3 May 1999 tornado. 21st Conf. on Severe Local Storms, San Antonio, TX, Amer. Meteor. Soc., 14.2, https://ams.confex.com/ams/SLS\_WAF\_NWP/ techprogram/paper\_47348.htm.
- —, T. Schuur, D. W. Burgess, and D. S. Zrnić, 2005: Polarimetric tornado detection. J. Appl. Meteor., 44, 557–570, https://doi.org/10.1175/JAM2235.1.
- Schultz, C. J., and Coauthors, 2012a: Dual-polarization tornadic debris signatures. Part I: Examples and utility in an operational setting. *Electron. J. Oper. Meteor.*, 13, 120–137.
- —, and Coauthors, 2012b: Dual-polarization tornadic debris signatures. Part II: Comparison and caveats. *Electron. J. Oper. Meteor.*, **13**, 138–150.
- Schuur, T. A., A. Rhzhkov, D. W. Burgess, and D. S. Zrnic, 2004: Polarimetric radar observations of tornadic debris signatures. 22nd Conf. on Severe Local Storms, Hyannis, MA, Amer. Meteor. Soc., 8B.3, https://ams.confex.com/ams/11aram22sls/techprogram/paper\_81504.htm.
- Snyder, J. C., and H. B. Bluestein, 2014: Some considerations for the use of high-resolution mobile radar data in tornado intensity determination. Wea. Forecasting, 29, 799–827, https:// doi.org/10.1175/WAF-D-14-00026.1.
- Tanamachi, R. L., H. B. Bluestein, J. B. Houser, S. J. Frasier, and K. M. Hardwick, 2012: Mobile, X-band, polarimetric Doppler radar observations of the 4 May 2007 Greensburg, Kansas, tornadic supercell. *Mon. Wea. Rev.*, 140, 2103–2125, https://doi.org/10.1175/MWR-D-11-00142.1.
- Trapp, R. J., D. M. Wheatley, N. T. Atkins, R. W. Przybylinski, and R. Wolf, 2006: Buyer beware: Some words of caution on the use of severe wind reports in postevent assessment and research. Wea. Forecasting, 21, 408–415, https://doi.org/10.1175/ WAF925.1.
- Umeyama, A., B. L. Cheong, S. Torres, and D. Bodine, 2018: Orientation analysis of simulated tornadic debris. J. Atmos. Oceanic Technol., 35, 993–1010, https://doi.org/10.1175/ JTECH-D-17-0140.1.
- Van Den Broeke, M. S., 2015: Polarimetric tornadic debris signature variability and debris fallout signatures. J. Appl. Meteor. Climatol., 54, 2389–2405, https://doi.org/10.1175/JAMC-D-15-0077.1.
- —, and S. T. Jauernic, 2014: Spatial and temporal characteristics of polarimetric tornadic debris signatures. *J. Appl. Meteor. Climatol.*, **53**, 2217–2231, https://doi.org/10.1175/JAMC-D-14-00941
- Wakimoto, R. M., and B. E. Martner, 1992: Observations of a Colorado tornado. Part II: Combined photogrammetric and Doppler radar analysis. *Mon. Wea. Rev.*, **120**, 522–543, https://doi.org/10.1175/1520-0493(1992)120<0522:OOACTP> 2.0.CO;2.
- —, N. T. Atkins, and J. Wurman, 2011: The LaGrange tornado during VORTEX2. Part I: Photogrammetric analysis of the

- tornado combined with single-Doppler radar data. *Mon. Wea. Rev.*, **139**, 2233–2258, https://doi.org/10.1175/2010MWR3568.1.
- ——, P. Stauffer, and W.-C. Lee, 2012: Finescale structure of the LaGrange, Wyoming, tornado during VORTEX2: GBVTD and photogrammetric analysis. *Mon. Wea. Rev.*, **140**, 3397– 3418, https://doi.org/10.1175/MWR-D-12-00036.1.
- —, N. T. Atkins, K. M. Butler, H. B. Bluestein, K. Thiem, J. Snyder, and J. Houser, 2015: Photogrammetric analysis of the 2013 El Reno tornado combined with mobile X-band polarimetric radar data. *Mon. Wea. Rev.*, 143, 2657–2683, https://doi.org/10.1175/MWR-D-15-0034.1.
- —, and Coauthors, 2016: Aerial damage survey of the 2013 El Reno tornado combined with mobile radar data. *Mon. Wea. Rev.*, **144**, 1749–1776, https://doi.org/10.1175/MWR-D-15-0367.1.
- ——, Z. Wienhoff, H. B. Bluestein, and D. Reif, 2018: The Dodge City tornadoes on 24 May 2016: Damage survey, photogrammetric analysis combined with mobile polarimetric radar data. *Mon. Wea. Rev.*, **146**, 3735–3771, https://doi.org/10.1175/MWR-D-18-0125.1.
- Wienhoff, Z. B., 2016: Doppler radar analyses of tornadic supercells on 19 May 2013. M.S. thesis, School of Meteorology, University of Oklahoma, 163 pp.
- ——, H. B. Bluestein, L. J. Wicker, J. C. Snyder, A. Shapiro, C. K. Potvin, J. B. Houser, and D. W. Reif, 2018: Applications of a

- spatially variable advection correction technique for temporal correction of dual-Doppler analyses of tornadic supercells. *Mon. Wea. Rev.*, **146**, 2949–2971, https://doi.org/10.1175/MWR-D-17-0360.1
- Wurman, J., 2002: The multiple-vortex structure of a tornado. *Wea. Forecasting*, **17**, 473–505, https://doi.org/10.1175/1520-0434(2002)017<0473:TMVSOA>2.0.CO;2.
- ——, and S. Gill, 2000: Finescale radar observations of the Dimmitt, Texas (2 June 1995), tornado. *Mon. Wea. Rev.*, **128**, 2135–2164, https://doi.org/10.1175/1520-0493(2000)128<2135: FROOTD>2.0.CO;2.
- —, and K. Kosiba, 2013: Finescale radar observations of tornado and mesocyclone structures. *Wea. Forecasting*, 28, 1157–1174, https://doi.org/10.1175/WAF-D-12-00127.1.
- —, and P. Robinson, 2013: In situ, Doppler radar, and video observations of the interior structure of a tornado and the wind-damage relationship. *Bull. Amer. Meteor. Soc.*, **94**, 835–846, https://doi.org/10.1175/BAMS-D-12-00114.1.
- —, —, and T. Marshall, 2014: The role of multiple-vortex tornado structure in causing storm researcher fatalities. *Bull. Amer. Meteor. Soc.*, **95**, 31–45, https://doi.org/10.1175/BAMS-D-13-00221.1.
- Zehnder, J. A., J. Hu, and A. Razdan, 2007: A stereo photogrammetric technique applied to orographic convection. *Mon. Wea. Rev.*, 135, 2265–2277, https://doi.org/10.1175/MWR3401.1.